Jay Baltisberger
Sabbatical Report
June 2011 to August 2012

Introduction

For my sabbatical leave during 2011-2012, I worked in the chemistry department at The Ohio State University in Columbus, Ohio with Dr. Philip Grandinetti, a leader in the field of glass structure and solid-state nuclear magnetic resonance (NMR) spectroscopy from June 2011 until August 2012. The original goal of my sabbatical was to study geology and work towards a thesis in this field so that I could one day teach geology courses at Berea College. In the absense of funding to pay for me to take classes in a degree program, I instead turned towards Professor Grandinetti who funded me to work as a visiting research professer in his group.

In the Fall 2011, my work in the Grandinetti lab did afford me the opportunity to audit geology courses in both Mineralogy and Introductory Geophysics. During the winter and spring, however, there was insufficient time available to take more classes since Philip was teaching two classes in the winter quarter and my time was needed in the lab on a regular basis. The research in the Grandinetti lab focussed on developing improved NMR methods to study amorphous materials. As often happens in research, our initial experiments led us to questions with surprising answers, in this case to a new technique we call phase incremented echo train acquisition (PIETA) that has potential that extends far beyond just solid-state NMR. While this change in the nature of my sabbatical was rather significant, the fundamental goal to improve my research and gain new skills that I can bring back to my classes at Berea remained and were accomplished. A number of the research projects were left unfinished but will be continued next summer in Orleans, France where I have been invited to work for a month and continuing at Berea College in coming years.

Project Narrative

One major goal of my sabbatical work at The Ohio State University was to develop my research skills and bring those back to enhance my own undergraduate research program at Berea College. Enhancing the research experience of undergraduates at Berea College will improve the overall chemistry program. In fact, during the summer of 2012, I was joined by Pyae Phyo, a first year chemistry student from Berea College, who was paid by Dr. Grandinetti this summer and she continues to work with me this academic year (and beyond if she finds the work productive.) In addition, I have made contacts with researchers in France with whom I will collaborate next

summer (2013) for a month as well as researchers in Brazil who have interest in our newly discovered pulse sequence. I will briefly describe the major research projects that I worked on at OSU, including attaching an electronic version of the already published *Journal of Chemical Physics* article from this year and drafts we are submitting shortly. There will also be additional articles that shall be published as a result of this research in coming years that will be described in the following sections.

Phase Incremented Echo Train Acquisition (PIETA)

One of the first problems that I worked on at OSU was adding Carr-Purcell-Meiboom Gill (CPMG) detection to a magic-angle flipping (MAF) experiment. This is an approach that others have studied and thankfully I ignored the newest (and ultimately flawed) work and set out to think about the problem with a fresh perspective. I say this because if I had blindly said "what do other people do in this case" then we would probably not have asked the questions about phase and pulses in CPMG that ultimately led us to a completely new approach called phase incremented echo train acquisition (PIETA). In traditional NMR experiments, the relative phases of the applied radiofrequency (RF) pulses are shifted to allow the desired signals to be coadded in a constructive manner and the undesired artifact signals in a destructive manner. This phase cycling approach has been applied to many different problems over the years, however in the case of CPMG, the phase cycle needed would grow exponentially with the number of applied pulses and required a difficult receiver phase shift for each acquired echo.

Previous work in the mid 1970s by Richard Ernst had shown that collecting data as a function of phase (and not just coadding these signals) could lead to advantages in the acquisition of multiple mixed coherence signals. This technique was not explored due to the lack of suitable computation and memory capacity in the computers of the era. Today we have far faster computers with ample storage and memory and revisiting the idea of a true phase dimension seemed worthwhile. In our studies we ultimately discovered that the time-proportional phase incrementation (TPPI) approach used by Pines in the late 1970s to do multiple quantum NMR could be modified to make our phase-incremented echo train acquistion scheme.

In this experiment the usual CPMG pulse sequence is used with changes in RF phase. The $\pi/2$ excitation pulse is applied with alternating 0° and 180° phase shifts with data coadded with a 0° and 180° phase shift as well. The odd numbered π pulses (first, third, fifth, etc.) are all given a phase shift that is (360° k / n) where k goes from 0 in the first experiment to n–1 in the last experiment for that dimension. The even π pulses are all given a phase of 90° or (90°, 90°, 270°,

270°) if we do a 4-step cycle on the first pulse. The data is then collected as a three dimensional format with dimension for t_2 acquisition, echo count and PIETA phase shift. When we do a Fourier Transform with respect to this PIETA phase, we get a result that looks like figure 1 (taken at the t_2 value with maximum signal).

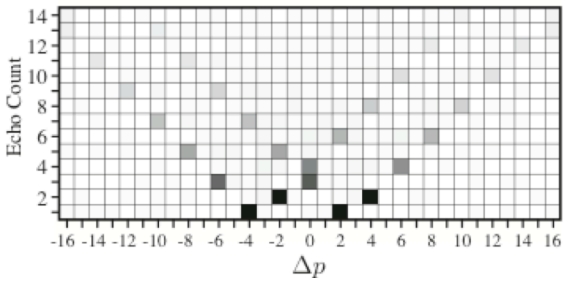

Figure 1. Diagram showing the separation of different coherence orders by PIETA as a function of echo number. This demonstrates how PIETA can be used to choose the desired coherence by performing a Fourier Transform with respect to phase rather than by co-addition of data sets in ways that are often impossible on most modern NMR spectrometers. Normally a spectrometer may only choose one column from this figure rather than choosing individual points as needed.

The graph in figure 1 shows that different coherence pathways (desired and undesired signals) have been successfully separated by this PIETA experiment. This allows us to choose a single point on this grid and process the t_2 dimension (a vector into the plane of the paper) as we would any other NMR data, but in this case we have guaranteed the pathway of the signal. This is critical if we wish to construct a signal where information in the echo count dimension matters such as J-spectroscopy or T_2 measurement. This is also critical if there are multiple signals present in one echo count row (as is the case in figure 1). Each of these may represent a signal that must be processed differently and may not be coadded until after processing. In this way we may collect multiple data sets that otherwise would require multiple experiments. The application of PIETA to T_2-weighted magnetic resonance imaging, diffusion/porous media spectroscopy, and solid-state NMR signal enhancement schemes like MQMAS-PIETA, MAT-PIETA, and QMAT-PIETA are all experiments that may lead to significant increase in popularity of PIETA in coming years. The initial results were published in an communication published in the *Journal of Chemical Physics* this spring and even was the most downloaded article for the month of June in that journal.

The article from our *Journal of Chemical Physics* article is included at the end of this report as Appendix A. The utility of the PIETA approach is shown in figure 2 where the J-resolved spectrum for a molecule of ethylbenzene is acquired in a

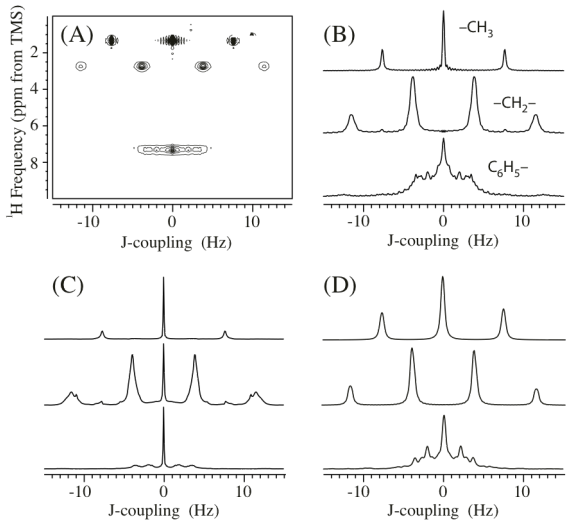

Figure 2. J-Resolved spectrum (A) of ethylbenzene comparing PIETA (B) to CPMG (C) along with a simulation of the slices from the 2D spectrum (D).

single scan (A & B) and compared to the same spectrum acquired with CPMG (C). The kinds of artifacts that are successfully removed are seen clearly in the 0 frequency spike in all three CPMG slices (C) pulled from the 2D spectrum. When we perform PIETA, we get a nearly perfect match between the observed slices (A) and the simulations (D) based on standard NMR signal theory. The slight difference between the bottom slice in these two is due to the lack of long range J-coupling information in the simulation.

Magic-Angle Turning (MAT) and Phase Adjusted Spinning Sidebands (PASS)

The second project that emerged from the PIETA work is combining this idea with the conventional solid-state NMR experiments of MAT and PASS. Both of these experiments have the fundamental goal of separating the isotropic chemical shift interaction from the chemical shift anisotropy (CSA) interaction. The historical approaches to do this are experiments called magic-angle hopping, magic-angle flipping, and dynamic angle spinning. In each of these the isotropic shift is correlated with a static (sometimes scaled by a factor of ½) lineshape in a second dimension. In all of these experiments the anisotropic resolution is limited due to residual dipolar interactions that limit utility to mostly dilute nuclear spins (^{13}C, ^{29}Si, etc.) Finally in these experiments the probe used to perform the work is not commercially available and must be custom-made which can be either costly or impossible for many labs.

The MAT and PASS versions of these correlation experiments give a spinning sideband manifold rather than a static powder pattern in the anisotropic dimension. This is useful for a variety of reasons; first the pattern is normally free of dipolar interactions that broaden and distort the pattern. Second, the experiment may be conducted using a standard magic-angle spinning (MAS) probe that may be purchased commercially. A serious difficulty encountered when trying to add CPMG detection to the PASS and MAT experiments (work done by a graduate student before I arrived at OSU). Essentially the phase modulation in one dimension became tangled in the echo train acquisition dimension. We quickly realized that PIETA would remove this entanglement and allow all echoes to be added to enhance signal-

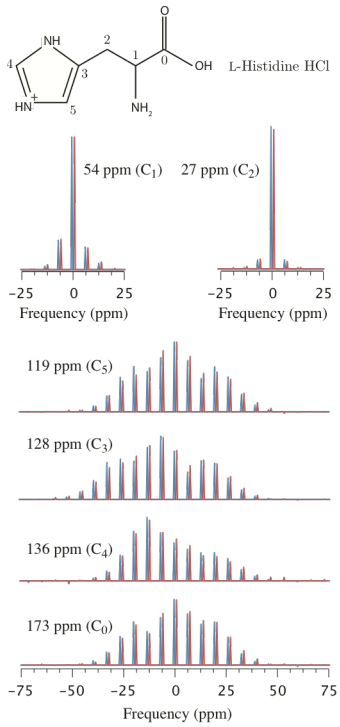

Figure 3. MAT-PIETA slices (shown in red) from ^{13}C spectrum of L-Histidine (a common amino acid). Simulations (shown in blue) match the spectra nearly perfectly and are in agreement (within error limits) with other experiments on the same sample.

to-noise ratios in PASS-PIETA experiments.

This work on PASS-PIETA was then generalized and we now understand the advantages and disadvantages of PASS-PIETA, QMAT-PIETA, and MAT-PIETA and how using a double-shear processing allows us to extract the maximum information in these experiments. This work is currently being submitted to the Journal of Chemical Physics (as was the first PIETA paper) and the draft is attached in the second appendix. Figure 3 is an example of MAT-PIETA applied to the ^{13}C resonances in L-Histidine. The sideband slices (shown in red) match the simulations (shown in blue) with very high precision and agree with other studies. The ease of setting up this experiment, combined with the speed of data acquisition and processing means the MAT-PIETA promises to be a highly cited technique.

Amorphous Materials

The other project area in the Grandinetti lab relates to studying amorphous materials, in particular silicate glasses. This has resulted in three major studies that will ultimately be published separately. The first of these is in the draft stage and is included as the third appendix to this report. Silicate glasses pose a challenge for any form of spectroscopy (NMR and others) since they possess only short and some medium range order, they generally give spectra that are quite featureless. It turns out that the magic-angle flipping (MAF) and magic-angle turning (MAT) experiments are some of the most informative in regards to the ^{29}Si sites in these glasses. Briefly, the structure of a silicate glass consists of many SiO_4 tetrahedra connected at the corners to make a three-dimensional (but random) lattice. When all silicate tetrahedra connect to other silicate tetrahedra (all oxygens are of the bridging variety) we describe these as $Q^{(4)}$ sites (meaning each silicon has four briding oxygens to other silicon atoms.) This lattice is interrupted when cations in the form of metal oxides (Na_2O, K_2O, MgO, PbO, etc.) are added to the glass. These cations break up the lattice to form non-bridging oxygen sites where a silicon is connected by three (or fewer) bridging oxygens to other silicon atoms and these are termed $Q^{(3)}$ and $Q^{(2)}$ sites. These cations may cause dramatic changes in fundamental properties of the glass

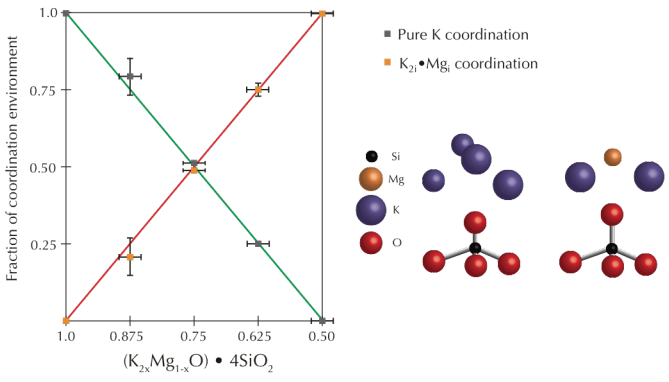

Figure 4. $Q^{(3)}$ binary site model for K/Mg mixed tetrasilicate glasses. The two site model suggests that a given non-bridging oxygen site is coordinated by a limited number of distinct possibilities.

including (but not limited to) melting point, glass transition temperature, enhanced chemical resistance, and index of refraction (for PbO glasses are remarkable in that they can have an index of refraction approaching that of materials like diamond.)

In our studies, we have focused mostly on glasses modified by alkali and alkaline earth elements (Na_2O, K_2O, MgO, SrO, etc.) In these materials an open question remains regarding the coordination of various cations and anions in the glasses. One of the projects involved synthesizing a series of tetrasilicate glasses bridging the composition from $K_2Si_4O_9$ to $KMg_{1/2}Si_4O_9$. This is a composition that we studied in 1992 at the University of California at Berkeley using ^{17}O dynamic-angle spinning and published in the journal *Nature*. In the current study we used ^{29}Si MAF to look at the $Q^{(3)}$ sites in these glasses (analagous to the non-bridging ^{17}O sites in the *Nature* study.) These results suggest that the high degree of cation ordering about the non-bridging oxygen sites is mirrored in the ^{29}Si MAF spectra where we find only two kinds of $Q^{(3)}$ sites corresponding to a K_2O rich region and a K_2O/MgO mixed cation region.

A second study involved looking at how various alkali and alkaline earth cations affect the chemical shift anisotropy for the $Q^{(3)}$ sites in tetrasilicate and disilicate glasses. The fundamental change introduced by varying the cation is to modify the charge on the cation and the ionic radius of the cation. With a larger cationic radius, the cation takes up more space in the structure of the glass and must be coordinated by a larger number of oxygen atoms (both bridging and non-bridging). In addition as the charge increases, the degree of covalent character in the bonding increases and makes the non-bridging oxygen atoms behave more like bridging oxygen atoms. Defining a cationic potential in terms of the charge on the cation divided by the ionic radius leads to a useful parameter that helps to differentiate the various bonding environments. A lower cation potential (coming from modifiers such as K_2O, Rb_2O, and Cs_2O) produces a shorter non-bridging oxygen bond length and a larger overall chemical shift anisotropy. Remarkably, we are able to see what appears to be differences in coordination environment with Cs_2O glasses showing showing multiple $Q^{(3)}$ sites. Given that these show a clear distinction between two types of sites, this implies once again

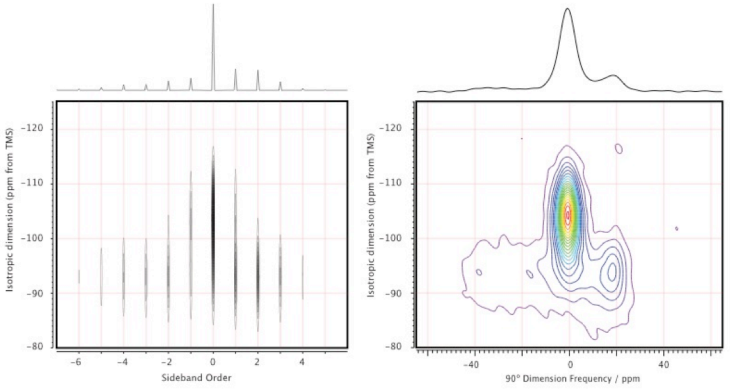

Figure 5. Comparison of MAT-PIETA and MAF-CPMG for a $K_2Si_4O_9$ glass, showing that both experiments may be used to extract comparable chemical shift anisotropy patterns.

that the cations are significantly more ordered than might previously have been supposed from molecular modeling experiments.

The final glass study focusses on using MAT-PIETA to replace the MAF-CPMG experiments. We have examined some of the same glasses from the other projects and have demonstrated that similar chemical shift anisotropy patterns may be extracted from both. This is quite important since the MAT-PIETA experiment may be used much more generally since it doesn't require any special probes to perform and in fact has higher net signal-to-noise ratios than the equal length MAF-CPMG experiment. We returned to the K/Mg mixed tetrasilicate glass to examine if the extracted CSA parameters from MAT are in agreement with those we extraced from the MAF experiment earlier. Figure 6 shows the spectra for each of the same five compositions studied in figure 4. In this case we simulated the two end member compositions with a single spinning pattern for each representing a pure K_2O coordination environment surrounding a $Q^{(3)}$ and the other a K_2O/MgO stoichiometric coordination envirionment. By mixing these two sideband patterns in ratios appropriate to the calculated fractions of the two $Q^{(3)}$ environments, we find that the simulations and data are in near perfect agreement. This suggests that using MAT instead of MAF is fully justified. We are in the process of extracting the experimental uncertainties in these parameters to compare the two approaches in a more numerically rigours manner. This seems promising and we plan to continue to perform MAT experiments at Berea College in coming years. Most of this work was performed with the assistance of Pyae Phyo, the research assistant from

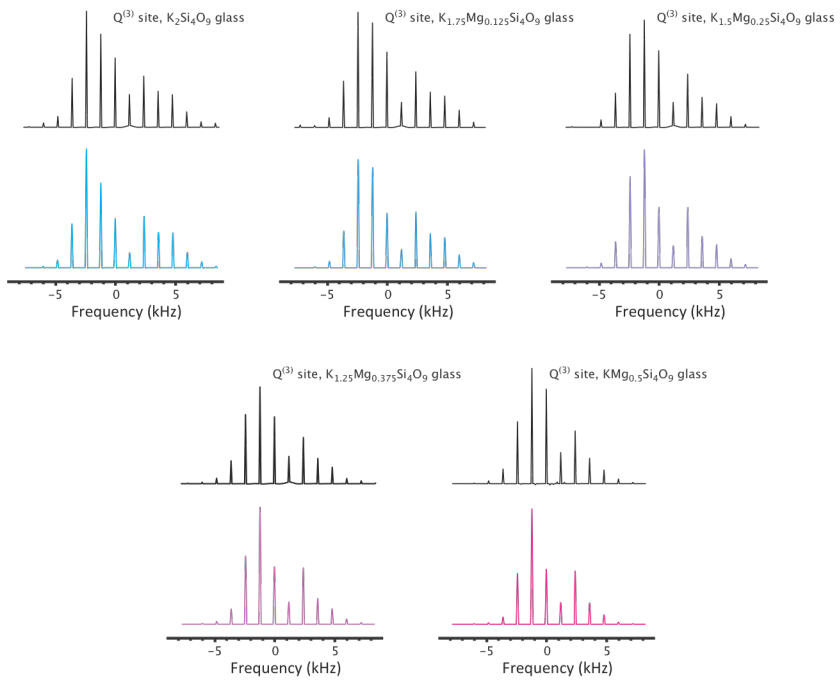

Figure 6. Experimental and simulated spinning sideband patterns for the range of K/Mg tetrasilicate glasses studied. Single site simulations were performed on the end members of this sequence and intermediate simulations were generated by weighted averaging of the two end members.

Berea who worked with me during the summer of 2012. The paper describing this work has not been written yet but will be something we are working on throughout the 2012-2013 academic year.

Educational Accomplishments

One of my major goals was to increase my understanding of geology and take courses in earth science that could be brought back to Berea College to be added to the sceince division offerings. Given that funding was not found to specifically take classes, I was happy to be able to audit the mineralogy course (as well as the lab portion) along with the introductory geophysics course. The most promising thing I found was the discussions with the geology faculty at OSU led me to ask if I really needed more coursework at all. Three different faculty basically told me that a PhD in physical chemistry was already close enough to the field of geology that I should just teach myself the material I want to cover in the introductory classes at Berea. They suggested that most of the introductory material of a geology curriculum is basically applied physical chemistry. Sitting in the mineralogy and geophysics courses reinforced this perspective as there was almost no material in these courses that I had not seen before. I would say the one hole that I need to fill is more field work and practice with sample identification. One of the geologists told me that even trained geologists get out of practice in this area and that basically she relearns it each time she faces new challenges in the field. I do believe that in the next few years the possibility of offering an introductory physical geology or mineralogy course is possible at Berea College. This is particularly true if chemistry staffing issues can be dealt with in a more permanent manner (given the revolving door of adjunct/visiting personnel we have had to cover the service courses.)

A second goal was to enhance my research and bring back projects that I can continue with undergraduate assistants at Berea College. In this regard the work was a smashing success in that we developed new techniques that will lend themselves well to be used in our own NMR spectrometer (PIETA, MAT-PIETA, and MQMAS-PIETA.) Also working with the OSU undergraduates (and graduate students) in the Grandinetti lab has convinced me that we can continue this work at Berea College and use our own undergraduates to do the same things they do up there. What is fundamentally needed is a commitment from the students to put in 10 hours or so of research each week. This also has encouraged me to change how we budget our NMR time on our own spectrometer to manage my research projects in a more productive way. Working with a rising sophomore (Pyae Phyo) has shown me that there are elements in my work that we really can pursue with students who have not had upper level courses. This is particularly true in working with T_2 experiments on pourous media that might lend itself nicely to the petroleum research fields.

Also as I work with researchers in France and Brazil in coming years, I am confident these projects will blossom into things we can do in Berea. In some ways the last 10 years since my previous sabbatical have been a blur between being the chemistry department chair and dealing with my wife's health. I think with more free time in my schedule, I will be able to really move research projects back into the forefront of my academic life.

The ultimate goal of any sabbatical has to be to improve my peformance as a faculty member at Berea College. Adding geology courses to the curriculum at some point certainly promises to enhance the educational opportunities for Berea College students. Increasing my research productivity will also certainly benefit our chemistry majors and aid them in efforts to build a strong curriculum vitae and get into good graduate and professional programs and ultimately into careers they will enjoy. Also, auditing the two geology courses at OSU helped me reconnect with what it is like to be a student again. It was enlightening to sit in the back and watch teaching methods that varied in success from great to terrible. I suppose this is possible to do at Berea College when I attend classes by my peers here, but it is difficult at Berea to separate the friendships I have with these faculty members from the observations. At OSU, I was able to be a more impartial observer and saw both positives and negatives. One approach that really impressed me was watching how the students responded to the mineralogy lab where the professor refused to give direct answers but instead answered questions with questions. I think at times we do too much direct answering the questions of our students at Berea College. Answering the questions with more questions seems to help build critical thinking skills. I ma not sure going to the extremes that were followed in that class was the best solution, but certainly this has me considering new ideas to try here at Berea College. In the bare minimum, seeing other faculty members in action does inspire new thinking down the road; in this regard my sabbatical has been overall a productive experience.

Conclusions

The overall goal of this project was to gain some research experience in some new MAS techniques and bring this research back to Berea College to help improve my research and teaching here. I ended up attending two professional meetings (the Experimental NMR Conference in Miami and the Glass and Optical Materials Division of the American Ceramics Society in St. Louis) and found that our new ideas were greeted with enthusiasm and should lead to further collaborations. Already Phil Grandinetti and I have been offered funding to work in France for a month in the summer of 2013 to pursue J-coupling and imaging experiments. Phil spent time in Brazil and a lab

there wants me to come down at some point and work with them on petroleum research problems with PIETA. We have published one paper already and have at least seven more that will be submitted in the coming year (MAT-PASS-PIETA, K/Mg MAF, Alkali MAF, MAT-MAF Comparison, d-p Echo, 2D Tenting Algorith for NMR Simulations, and MQMAS-PIETA). There are further projects in the works that will also end up producing publications in the imaging community, the inhomogenous porous media community, as well as continuing experiments in the amorphous materials community. The impact of auditing geology courses will enhance my teaching of both new courses in the earth science field as well as encouraging me to experiment with new pedagody in my current chemistry courses. I was initially very disappointed that I could not find funding to do a mostly educational project in geology at the University of Kentucky. When Philip Grandinetti hired me as a visiting professor for the last 15 months, it proved to be one of the most productive research periods of my career (dating back to graduate school when I worked with Philip as a graduate student and he was a post-doc in the Pines lab.) I may have had to abbreviate my geology experiences but the trade-off was ultimately beneficial as we made discoveries that ultimately may prove to be very highly cited (as one reviewer of the first PIETA paper suggested).

Appendix A

Phase Incremented Echo Train Acquisition in NMR Spectroscopy

Jay H. Baltisberger,[1] Brennan J. Walder,[2] Eric G. Keeler,[2] Derrick C. Kaseman,[2] Kevin J. Sanders,[2] and Philip J. Grandinetti[2]

[1)] *Division of Natural Science, Mathematics, and Nursing, Berea College, Berea, Kentucky 40403*

[2)] *Department of Chemistry, Ohio State University, 100 West 18th Avenue, Columbus, OH 43210, USA*[a)]

(Dated: 1 May 2012)

We present an improved and general approach for implementing Echo Train Acquisition (ETA) in magnetic resonance spectroscopy, particularly where the conventional approach of Carr-Purcell-Meiboom-Gill (CPMG) acquisition would be too complicated or impossible. Generally, adding ETA to any N-dimensional experiment creates an $N+1$ dimensional experiment, with an additional dimension associated with the echo count, n, or an evolution time that is an integer multiple of the spacing between echo maxima. Here we present a modified approach, called Phase Incremented Echo Train Acquisition (PIETA), where the phase of the mixing pulse and every other refocusing pulse, ϕ_P, is incremented as a single variable, creating an additional phase dimension in what becomes an $N+2$ dimensional experiment. A Fourier transform with respect to the PIETA phase, ϕ_P, converts the ϕ_P dimension into a Δp dimension where desired signals can be easily separated from undesired coherence transfer pathway signals, and thereby avoiding cumbersome or intractable phase cycling schemes where the receiver phase must follow a master equation. This simple modification eliminates numerous artifacts present in NMR experiments employing CPMG acquisition allowing "single-scan" measurements of transverse relaxation and J-couplings. Additionally, unlike CPMG, we show how PIETA can be appended to experiments with phase modulated signals after the mixing pulse.

Keywords: NMR spectroscopy, echo train acquisition, J-resolved spectroscopy, relaxation, diffusion, imaging

Echo Train Acquisition (ETA) is a powerful approach in magnetic resonance, forming the basis of a number of diverse and advanced magnetic techniques, such as Echo Planar Imaging[1] in MRI, diffusion and transverse relaxation measurements[2–6], ultra-fast multi-dimensional liquid state NMR[7], and sensitivity enhancement in solid-state NMR[8]. The primary benefits of ETA are reduced experiment time, enhanced sensitivity, and the ability to separate frequency contributions that are refocused during the echo train pulse sequence from those that are not. Here we present an improved method, called Phase Incremented Echo Train Acquisition (PIETA) for adding ETA to a number of NMR experiments where the standard approach of Carr-Purcell-Meiboom-Gill (CPMG) acquisition would be too complicated or impossible to implement.

In CPMG acquisition, shown in Fig. 1A, a train of rf pulses produces a train of echo signals arising from the refocusing of frequency contributions with odd symmetry in their spin transition function[9]. Frequency contributions lacking odd symmetry result in a modulation or decay of the echo train signal. In principle, the echo amplitude modulations in liquid-state CPMG experiments could be used to measure unrefocused J coupling frequency contributions when the size of the couplings is smaller than the line width from magnetic field inhomogeneities[10]. Additionally, the echo amplitude decays in CPMG could be related to transverse relaxation rates independent of molecular diffusion rates[2,3]. It is well known[11,12], however, that CPMG can often fail to produce desired results because of non-ideal rf pulses introducing contaminating signals from undesired coherence transfer pathways.

Ideally, each echo observed in a CPMG experiment is the result of a coherence transfer from $p=+1 \rightarrow -1$ by a single rf pulse. If the rf pulse creating the transfer is a perfect π rotation of the magnetization, then the efficiency of this transfer is 100%. Unfortunately, resonance offset effects, as well as rf field inhomogeneities, lead to inefficient transfers. Thus, coherences may "leak" into undesired pathways, i.e., $p=+1 \rightarrow 0$ and $p=+1 \rightarrow +1$. In ETA even the smallest inefficiencies lead to significant signal loss since the intensity of the echo after n transfers is reduced by the transfer efficiency to the nth power. While these intensity losses are real, they are generally unobservable because they are "buried" under undesired echo signals coming from various stimulated echoes, that is, the undesired pathways. This effect leads to multi-exponential CPMG echo decays in situations where perfect π pulses would yield only a single exponential[4]. Additionally, any attempts to measure J couplings from the modulation of the CPMG echo train amplitude become intractable because of signal contamination from undesired pathways.

Clearly, a challenge in using ETA acquisition is in obtaining perfect refocusing and eliminating undesired signal pathways. In CPMG, one can strive for perfect π pulses through higher rf powers and restricting the sample to the most homogeneous part of the rf transmitter coil, although these approaches have drawbacks. For example, smaller rf coils can provide a higher rf

[a)] http://www.grandinetti.org

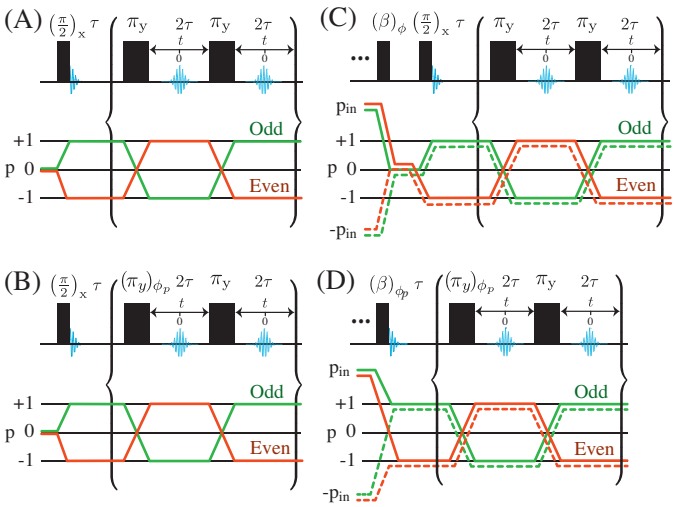

FIG. 1. In (A) is the original CPMG acquisition sequence[3]. In (B) is the PIETA sequence that replaces the CPMG sequence in (A). In (C) is how CPMG acquisition is appended to a sequence with a phase modulated coherence of order $p_{\rm in}$ prior to being converted into observable coherence of $p = -1$. With CPMG acquisition, the input coherence must pass through a $p = 0$ level (z-filter) and be converted into amplitude modulated signal before acquisition. In (D) is how PIETA is appended to a sequence with a phase modulated coherence of order $p_{\rm in}$ prior to mixing down for acquisition. Because PIETA does not have the z-filter requirement it can separate degenerate pathways where CPMG acquisition cannot, and additionally, gains a $\sqrt{2}$ improvement in sensitivity over CPMG acquisition.

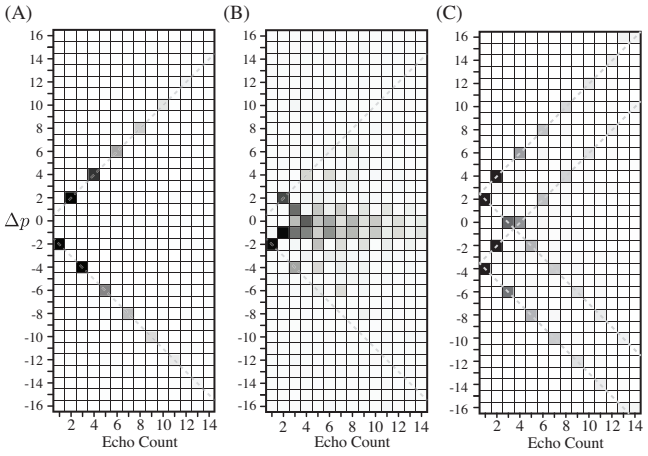

FIG. 2. Experimental 2D PIETA cross sections taken through the time origin. In (A) is a MAS-PIETA cross section of $RbNO_3$ using the sequence in Fig. 1B, where the π pulse width has been calibrated and no undesired pathway signals are observed. The Δp range from -16 to +16 was obtained using $\Delta\phi_P = 2\pi/32$. The cross-section in (B) was obtained with the same sequence and sample as (A) except the refocusing pulse was intentionally mis-set to $\pi/2$ to illustrate the presence of undesired pathway signals. (C) Experimental 2D cross section taken through the echo maximum at $t_1 = 0$ and $t_2 = 0$ in a 4D MQMAS-PIETA spectrum of $RbNO_3$ using $\Delta\phi_P = 2\pi/32$.

field strength but at the price of smaller sample volume, which, coupled with sample restriction, can be severely limiting for sensitivity. While perfect refocusing pulses in CPMG are the panacea to the problems described above, a significant subset of these problems can be solved by simply eliminating the undesired coherence transfer pathways. While the most obvious solution, proposed decades ago by Bain[13] and Bodenhausen et al[14], would be to cycle the pulse and receiver phases during signal coaddition according to a master equation to eliminate the undesired coherence transfer pathways, this approach cannot be easily applied to CPMG acquisition because the phase cycle for n refocusing pulses is, at minimum, on the order of 2^n steps. Thus, no pulse sequence using CPMG acquisition, even with "cogwheel" phase cycling[15], has been published that eliminates these artifacts. Since every observed echo can have contributions from multiple pathways, the challenge is to find a master equation for the receiver phase as a function of echo count that aliases all desired pathway signals away from undesired pathway signals.

Here we present a simple solution, based on the seminal work of Drobny et al[16], which exploits the signal as a function of ϕ_P, the pulse phase, being the Fourier conjugate of the signal as a function of Δp, the coherence order change during the pulse[17]. Generally, in ETA, an N-dimensional experiment becomes an $N+1$ dimensional experiment, with an additional dimension associated with the echo count, n, or an evolution time that is an integer multiple of the spacing between echo maxima. In PIETA, the mixing pulse and every other refocusing pulse are incremented by a phase, $\Delta\phi_P$, creating an $N+2$ dimensional experiment with the additional phase dimension. A Fourier transform with respect to the PIETA phase, ϕ_P, converts the ϕ_P dimension into a Δp dimension. The simplest application of PIETA, shown in Fig. 1B, is after a $\pi/2$ excitation pulse, which leads to a 3D signal, $S(t, n, \Delta p)$. Shown in Fig. 2A is the experimental 2D cross-section at $t = 0$ for such a signal in the case of the ^{87}Rb magic-angle spinning (MAS) NMR signal of polycrystalline $RbNO_3$. As can be seen in Fig. 2A, the PIETA cross-section with the Δp and n dimensions contains a "V" pattern of intensity from the desired pathways. The signals in the "squares" belonging to the desired pathways are extracted into a 2D signal as a function of t and n. If there is no frequency modulation along the n dimension, then one might further reduce the signal in a weighted average to maximize sensitivity[18] into a 1D signal as a function of t. In Fig. 2B, the refocusing pulse was intentionally mis-set to $\pi/2$ to make more prominent the undesired pathway signals, which appear inside the pattern of the desired pathway signals. The undesired pathway signals arise from stimulated echoes

and decay at a slower rate than the desired pathway signal.

Another important advantage of PIETA is that it can be appended to experiments with a phase modulated signal after the mixing pulse. This is in contrast to appended CPMG acquisition, illustrated in Fig. 1C, which requires any phase modulated coherence of order $p_{\rm in}$ to be converted into amplitude modulation via a z-filter before conversion into observable coherence of $p = -1$. As illustrated in Fig. 1D, PIETA can be appended to any phase modulated coherence without a z-filter requirement. For this reason, PIETA also gives a $\sqrt{2}$ improvement in sensitivity over CPMG acquisition and can separate degenerate pathways that CPMG acquisition cannot.

While this use of a concerted phase increment is similar to "cogwheel", the PIETA approach does not require a detailed analysis of the undesired pathways and the derivation of a master equation for the receiver phase. In fact, a PIETA spectrum can illustrate why no single master equation in conventional or "cogwheel" phase cycling will work for some experiments. This is seen when combining PIETA with the 2D MQ-MAS experiment[19]. Shown in Fig. 2C is the PIETA cross-section for the two pulse MQ-MAS experiment[20] combined with PIETA. In this experiment the phase modulated input coherence before mixing is $p_{\rm in} = -3$. The acquisition of both pathway and anti-pathway signals for hypercomplex acquisition in t_1 results in a doubled PIETA pattern. While reducing this 4D signal of $S(t_1, t_2, n, \Delta p)$ down to the 2D signal, $S(t_1, t_2)$, is straightforward, it is not immediately clear how one can derive a receiver master equation for coaddition of signals which can be implemented on existing commercial spectrometer hardware using available phase cycling schemes.

Finally, PIETA can reduce errors in measuring transverse relaxation rates and J-couplings. Additionally, it can provide this information in a "pseudo-single-scan" experiment. "Single-scan" in the sense that the entire multi-dimensional time domain signal is acquired in a single acquisition, and "pseudo" because the separate "single-scan" signals must also be acquired along an excitation phase dimension. Sampling in the excitation phase dimension, however, need not increase the total experiment time since it is performed in lieu of conventional phase cycling and signal averaging.

This approach is illustrated with the 2D J PIETA ^{1}H spectrum for ethylbenzene in Fig. 3A and its 1D cross sections in Fig. 3B. The multiplet structures and intensities are as expected and in good agreement with the simulated 2D cross sections for ethylbenzene shown in Fig. 3D. In contrast, the 1D cross sections obtained from a 2D J CPMG ^{1}H spectrum, shown in Fig. 3C, exhibit sharp zero frequency artifacts. Even in the presence of pulse imperfections the echo decays measured with PIETA exhibit a mono-exponential decay while CPMG echoes exhibit a multi-exponential decay[21]. Thus, PIETA is more robust with regards to rf pulse imperfections than CPMG in measuring transverse relaxation rates and J-couplings.

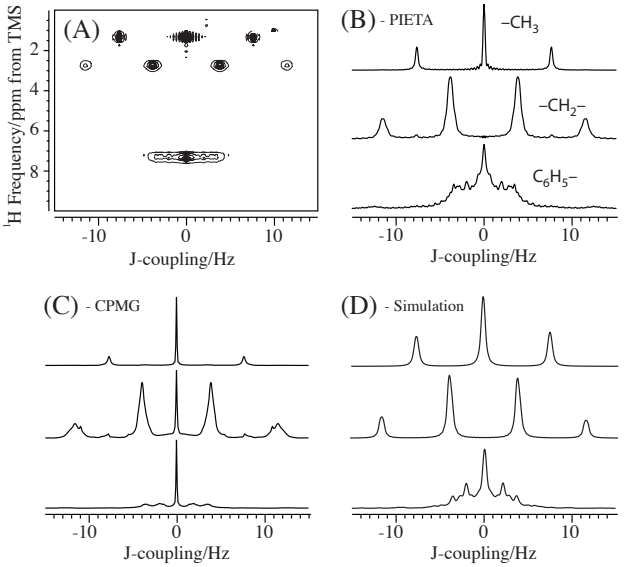

FIG. 3. (A) The 2D ^{1}H J spectrum of 10% ethylbenzene dissolved in $CDCl_3$ using PIETA using $\Delta\phi_P = 2\pi/128$. Comparison of 2D cross sections from (B) 2D J PIETA and (C) 2D J CPMG. In both the CPMG and PIETA cross sections there are small intensity sinc function artifacts related to the truncation of signal inside the constant time acquisition between the π pulses. The simulated 2D cross sections for ethylbenzene shown in (D). Simulation parameters and details are given in the supplementary material[17].

Although, the echo decay in PIETA is mono-exponential, it still is vulnerable to pulse imperfections and the observed decay arises from both T_2 and cumulative coherence transfer inefficiencies.

In summary, PIETA can replace CPMG in every instance with little increase in experiment time, some additional signal processing steps, and significantly reduced artifacts. Additionally, unlike CPMG, PIETA can be appended to multi-dimensional NMR experiments with signals phase modulated from indirect evolution periods. Finally, PIETA opens the door to greater opportunities for the use of echo train acquisition in "pseudo-single-scan" 2D NMR spectroscopy. We believe this new approach will prove useful in a numerous applications such as solution-state NMR of biological molecules[5], solid-state NMR J spectroscopy in non-crystalline solids[22], improved MRI contrast[6], and mobile single-sided type NMR applications[23] such as oil-well logging[24].

ACKNOWLEDGMENTS

This material is based upon work supported by the National Science Foundation under Grant No. NSF CHE-1012175.

[1] P. Mansfield, "Multi-planar image formation using NMR spin

echoes," Journal of Physics C: Solid State Physics **10**, L55 – L58 (1977).

[2]H. Y. Carr and E. M. Purcell, "Effects of diffusion on free precession in nuclear magnetic resonance experiments," Phys. Rev. **94**, 630–638 (1954).

[3]S. Meiboom and D. Gill, "Modified spin-echo method for measuring nuclear relaxation times," Rev.Sci.Instrum **29**, 688 (1958).

[4]G. Gaelman and M. G. Prammer, "The CPMG pulse sequence in strong magnetic field gradients with applications to oil-well logging," J. Magn. Reson. A **113**, 11–18 (1995).

[5]A. Ross, M. Czisch, and G.C.King, "Systematic errors associated with the CPMG pulse sequence and their effects on motional analysis of biomolecules," J. Magn. Reson. **124**, 355–365 (1997).

[6]W. Foltz, J. Stainsby, and G. Wright, "T_2 accuracy on a whole-body imager," Magn. Reson. Medicine **38**, 759–768 (1997).

[7]L. Frydman, T. Scherf, and A. Lupulescu, "The acquisition of multidimensional nmr spectra within a single scan," Proceedings of the National Academy of Sciences of the United States of America **99**, pp. 15858–15862 (2002).

[8]N. M. Szeverenyi, A. Bax, and G. E. Maciel, "Magic-angle hopping as an alternative to magic-angle spinning for solid-state NMR," J. Magn. Reson. **61**, 440 (1984).

[9]P. J. Grandinetti, J. T. Ash, and N. M. Trease, "Symmetry pathways in solid-state NMR," Prog. N.M.R. Spect. **59**, 121–196 (2011).

[10]R. Freeman and H. D. W. Hill, "High-resolution study of nmr spin echoes: ''*J* spectra'','' J. Chem. Phys. **54**, 301–313 (1971).

[11]G. Gaelman and M. G. Prammer, "Analysis of carr-purcell sequences with nonideal pulses," J. Magn. Reson. B **109**, 301–309 (1995).

[12]Y.-Q. Song, "Categories of coherence pathways for the CPMG sequence," J. Magn. Reson. **157**, 82–91 (2002).

[13]A. D. Bain, "Coherence levels and coherence pathways in NMR. a simple way to design phase cycling procedures," J. Magn. Reson. **56**, 418–427 (1984).

[14]G. Bodenhausen, H. Kogler, and R. R. Ernst, "Selection of coherence-transfer pathways in NMR pulse experiments," J. Magn. Reson. **58**, 370–388 (1984).

[15]M. H. Levitt, P. K. Madhu, and C. E. Hughes, "Cogwheel phase cycling," J. Magn. Reson. **155**, 300–306 (2002).

[16]G. Drobny, A. Pines, S. Sinton, D. Weitekamp, and D. Wemmer, "Fourier transform multiple quantum nuclear magnetic resonance," Symp. Faraday Soc. **13**, 93 (1980).

[17]"See supplementary material,".

[18]K. Dey, J. T. Ash, N. M. Trease, and P. J. Grandinetti, "Trading sensitivity for information: CPMG acquisition in solids," J. Chem. Phys. **133**, 05401–01–054501–10 (2010).

[19]L. Frydman and J. S. Harwood, "Isotropic spectra of half-integer quadrupolar spins from bidimensional magic-angle spinning NMR," J. Am. Chem. Soc. **117**, 5367–5369 (1995).

[20]D. Massiot, B. Touzo, D. Trumeau, J. P. Coutures, J. Virlet, P. Florian, and P. J. Grandinetti, "Two-dimensional magic-angle spinning isotropic reconstruction sequences for quadrupolar nuclei," Solid State NMR **6**, 73–83 (1996).

[21]R. L. Vold, R. R. Vold, and H. E. Simon, "Errors in measurements of transverse relaxation rates," J. Magn. Reson. **11**, 283–298 (1973).

[22]P. Florian, F. Fayon, and D. Massiot, "^2J Si–O–Si scalar spin-spin coupling in the solid state: Crystalline and glassy wollastonite $CaSiO_3$," J. Phys. Chem. C **113**, 2562–2572 (2009).

[23]B. Blümich, J. Perlo, and F. Casanova, "Mobile single-sided NMR," Prog. NMR Spect. **52**, 197–269 (2008).

[24]Y.-Q.Song, H. Cho, T. Hopper, A. E. Pomerantz, and P. Z. Sun, "Magnetic resonance in porous media: Recent progress," J. Chem. Phys. **128**, 052212–1–12 (2008).

Appendix B

Affine Transformations of NMR Signals from Rotating Samples

Brennan J. Walder,[1] Krishna K. Dey,[1] Derrick C. Kaseman,[1] Jay H. Baltisberger,[2] and Philip J. Grandinetti[1, a)]
[1)] *Department of Chemistry, Ohio State University, 100 West 18th Avenue, Columbus, OH 43210, USA*
[2)] *Division of Natural Science, Mathematics, and Nursing, Berea College, Berea, Kentucky 40403*

(Dated: 21 September 2012)

An intuitive approach is presented for understanding and designing magnetic resonance experiments on rotating samples. The signal arising from such experiments can be described in the context of a two-dimensional coordinate system where the signal arising from rotor-modulated frequencies evolve along one coordinate, ϵ_m, whereas the signal arising from unmodulated frequencies evolve along the other coordinate, ϵ_u. Affine transformations relate the two-dimensional signals acquired in experiments such as Magic-Angle Turning (MAT) and Phase Adjust Spinning Sidebands (PASS) experiments to this common coordinate system. Depending on sequence design and acquisition conditions two significant artifacts can arise from truncated acquisition time and discontinuous damping in the T_2 decay. Here we show that a double shear affine transformation can eliminate the artifact arising from truncated acquisition time. An illustrative example of this approach is given for the ^{13}C MAT spectrum in L-Histidine. We also explain how the discontinuous damping artifact is eliminated when the NMR experiment is designed with pure rotor modulated frequency evolution occurring during a constant time period. Additionally, it is also shown that special care must be taken when applying the discrete Fourier transform to avoid introducing a third type of baseline signal artifact which arises because the 2D dimensional signal is periodic along the along the ϵ_m coordinate, but aperiodic along the ϵ_u coordinate. Finally, a general approach for combining phase incremented echo-train acquisition (PIETA) with MAT and PASS is described. This approach is applicable whenever strong inhomogenous broadenings dominate the unmodulated frequency resonances, such as in non-crystalline solids or in samples with large residual frequency anisotropy. PIETA provides significant sensitivity enhancements while also eliminating spectral artifacts would normally be present with CPMG acquisition. The PIETA experiments are demonstrated in the case of ^{29}Si in a $KMg_{0.5}O_2 \cdot 4SiO_2$ glass and in the case of the central transition of ^{87}Rb in polycrystalline Rb_2SO_4.

PACS numbers: Valid PACS appear here
Keywords: magnetic resonance, spinning sidebands, rotating samples, nuclear shielding anisotropy, nuclear quadrupolar coupling, imaging, PASS, MAT, PIETA, TOP processing

I. INTRODUCTION

When a sample rotates in a magnetic field, its magnetic resonance spectrum splits into a centerband resonance flanked by spinning sidebands at integer multiples of the spinning speed[1]. While spinning sideband resonances are often perceived as a spectral complication to be eliminated, they also contain valuable information about the frequency anisotropy[2]. For example, in solid-state Magic-Angle Spinning (MAS) NMR spectra of spin 1/2 nuclei the rotor-modulated frequency contribution provides information about the 2nd-rank chemical shift frequency anisotropy, whereas the unmodulated frequency contribution is the isotropic (0th-rank) chemical shift. In a similar way the dipolar coupling and nuclear electric field gradient for coupled nuclei and quadrupolar nuclei, respectively, can be measured. In magnetic resonance imaging, a separation of modulated and unmodulated frequency contributions while a sample rotates in a magnetic field gradient can be used to reconstruct a three-dimensional image of the sample within the rotor[3–5].

Since the seminal work of Dixon[6], various methods for separating the modulated and unmodulated contributions to a transition frequency in a rotating sample have been proposed. The central idea behind these methods is a recognition that the signal phase contributions from both rotor-modulated and unmodulated frequencies, which are parametrically dependent on the same time variable, can be separated by splitting their evolution into orthogonal time dimensions. Dixon showed in a detailed theoretical analysis that the solution of a set of simultaneous non-linear equations can provide the timings for a series of π pulses in the Phase Adjust Spinning Sidebands (PASS) experiment for separating the signal phase evolution arising from rotor-modulated and unmodulated frequencies. Unfortunately, the physical picture behind Dixon's discovery was not entirely obvious, and further refinement of his ideas languished for a number of years. Shortly after Dixon, however, Maciel and coworkers[7] developed an related approach called magic-angle hopping (MAH) for separating isotropic and anisotropic contributions of spin 1/2 nuclei. Their approach was physically intuitive as it was based on simple

[a)] http://www.grandinetti.org

symmetry arguments[8,9]. In subsequent years, a sequence of refinements to MAH dramatically improved its utility. First, Gan[10] realized that hopping could be replaced with slow turning without compromising the separation of isotropic and anisotropic contributions. Next, Grant and coworkers[11] and Pines and coworkers[12] showed that the sensitivity of Gan's magic-angle turning (MAT) experiment could be improved by using π pulses instead of $\pi/2$ pulses to eliminate undesired transverse evolution. During this period, Levitt and coworkers[13] began a detailed analysis of Dixon's approach and showed that both PASS and MAT are solutions to Dixon's equations with different boundary conditions. A thorough review of such solutions are described by Antzutkin[14]. Note that Antzutkin refers to the family of MAT solutions in his review as Isotropic Rotation Sequences (IRS).

The fundamental difference between the π pulse version of MAT and Levitt's version of PASS is that the former has a constant-time-indirect dimension for unmodulated (e.g., isotropic) frequency evolution while the latter has a constant-time-indirect dimension for modulated (e.g., anisotropic) frequency evolution. Because the rotor-modulated frequency evolution is periodic with the rotor period, Levitt and coworkers argued that sideband signal phase evolution is the natural choice for the constant time indirect dimension. This idea was further strengthened by the failure of MAT methods to provide an unmodulated frequency evolution dimension without signal artifacts arising from truncated acquisition and discontinuous signal damping in the unmodulated frequency evolution dimension[15]. Thus, PASS appears to be the more robust of the two approaches, although the complicated π pulse timings needed for PASS make it more challenging to implement on older commercial NMR spectrometers.

In previous work[16] we have shown that the direct and indirect dimensions of a 2D PASS experiment can be interchanged in a signal processing step: a double shear transformation called TOP. The TOP transformation swaps the sampling intervals in the direct dimension and indirect dimensions. This allows the sampling interval in the rotor-modulated evolution dimension of PASS to be taken from the direct dimension, typically allowing a significant reduction in the minimum time required to perform a PASS experiment. Here we show that the TOP transformation can also be applied to a MAT signal to eliminate its truncated acquisition artifact. A similar idea, using shifting acquisition periods instead of a post-acquisition signal transformation, has recently been described by Gan and coworkers[17,18]. We also demonstrate here how echo train acquisition can be appended to either PASS or MAT with equal gains in sensitivity. In contrast to recent claims[18] that echo train acquisition cannot be appended to PASS with the same sensitivity gain as MAT, here we show that a solution comes in realizing that the train of echo-refocusing π pulses must be equally spaced and positioned at times where the sum of the indirect and direct rotor modulated evolution time is an integer number of rotor periods.

Finally, because both PASS and MAT have phase modulated signals before detection, the conventional echo train acquisition approach of CPMG can result in signal artifacts from undesired coherence transfer pathways unless a z filter or complicated phase cycle with multiplex acquisition is implemented[18]. Here we present simpler approach based on the recently introduced "Phase Incremented Echo Train Acquisition" (PIETA) technique[19], which eliminates the need for a z filter or such multiplex acquisition schemes.

II. EXPERIMENTAL

Approximately 2g of $KMg_{0.5}O_2 \cdot 4SiO_2$ glass was synthesized from K_2CO_3 (Aldrich, 99+%), MgO (Alfa Aesar, 99.95%), SiO_2 (Aldrich, 99.995%), and CuO (Mallinckrodt). Prior to synthesis the K_2CO_3 and MgO were placed in a dehydrating furnace at 150°C overnight to remove any water from the sample. The starting materials were ground and placed in a furnace at 600°C overnight to decarbonate followed by melting at 1400°C for 1.5 hours. Each sample was quenched by placing the bottom of the platinum crucible in water. Each sample was ground into a powder and packed in a rotor in a nitrogen filled glove bag.

All NMR experiments were performed on a Bruker Avance operating at a field strength of 9.4 Tesla, utilizing spectrometer frequencies of 100.737 MHz for ^{13}C, 400.586 MHz for ^{1}H, 79.577 MHz for ^{29}Si, and 131.072 MHz for ^{87}Rb. All four-dimensional PIETA signals were reduced down to two dimensions, eliminating the PIETA phase and echo count dimensions as described elsewhere[19]. After TOP processing,four repeats of the acquired 2D signal in the periodic modulated evolution dimension was performed to separate sidebands. Signal-to-noise calculations, however, were based on spectra processed with no signal repeats to avoid an artificial boost of the sensitivity.

The MAT pulse sequence shown in Fig. 1 was performed on L-Histidine monochloride monohydrate (Sigma Aldrich) using a commercial Bruker 7 mm double resonance MAS probe with a rotor frequency of 1250 ± 2 Hz. The indirect dimension was incremented from $-t_R/2$ to $t_R/2$ in 32 steps. The phase dimension was incremented in steps of $2\pi/16$. The rf field strength of ^{1}H were 20 kHz and 35 kHz for initial excitation and TPPM decoupling, respectively. The rf field strength during ^{1}H-^{13}C cross-polarization was 19.2 kHz and the contact time of 0.6 ms was used. 24 scans per phase slice were collected at a recycle delay of 6 s. The total experiment time was 20 hr 32 min.

The MAT-PIETA pulse sequence, shown in Fig. 6, was performed on a sample of Cu(II) doped $KMg_{0.5}O_2 \cdot 4SiO_2$ glass using a commercial Bruker 7 mm double resonance MAS probe with a rotor frequency of 790 ± 1 Hz. The indirect dimension was incremented

from $-t_R/2$ to $t_R/2$ in 32 steps. The phase dimension was incremented in steps of $2\pi/128$. The rf field strength for all pulses on ^{29}Si was 50.8 kHz. The recycle delay used was 20 s, with one scan per PIETA phase increment. The total experiment time was 23 hr 6 min.

The shifted-echo QMAT and QMAT-PIETA pulse sequences applied to polycrystalline Rb_2SO_4 (Aldrich) were identical those shown in Fig. 2 and Fig. 6, except the five π pulse preparation was replaced with a nine π pulse preparation described elsewhere[20,21]. Experiments were performed in a Bruker 4 mm MAS probe spinning at 2604 ± 1 Hz. An rf field strength of 30 kHz was used for selective excitation of the central transition. The indirect dimension was incremented from $-t_R/2$ to $t_R/2$ in 32 steps. The phase dimension was incremented in steps of $2\pi/64$. 12 scans per PIETA phase increment were collected at a recycle delay of 0.75 s. The total experiment time was 5 hr 55 min.

III. RESULTS AND DISCUSSION

A. Background

The NMR transition frequency becomes time dependent during sample rotation. A multipole expansion of this frequency can be separated into rotor-modulated and unmodulated components:

$$\Omega(\phi_R) = \sum_{l=0}^{L_{\max}} \omega_{l,0} + \sum_{l=1}^{L_{\max}} \sum_{\substack{k=-l \\ k\neq 0}}^{l} \omega_{l,k} e^{ik\phi_R}, \qquad (1)$$

where ϕ_R is the rotor phase and $L_{\max}$ is the highest rank of spatial anisotropy contributing to the NMR frequency. The rotor phase advances under sample rotation according to

$$\phi_R = \omega_R t + \chi_R, \qquad (2)$$

where ω_R is the rotor frequency, t is the duration of rotation, and χ_R is the initial rotor phase.

After an excitation pulse the phase of the NMR signal for a rotating sample is given by

$$\Phi(t) = \int_0^t \Omega(\omega_R t' + \chi_R)\, dt', \qquad (3)$$

where t is the signal evolution time after the pulse. Substituting Eq. (1) into Eq. (3) one obtains

$$\Phi(t) = W_0 t + \sum_{l=1}^{L_{\max}} \sum_{\substack{k=-l \\ k\neq 0}}^{l} W_{l,k}(\chi_R) \left[e^{ik\omega_R t} - 1\right] \qquad (4)$$

where we have defined

$$W_0 = \sum_{l=0}^{L_{\max}} \omega_{l,0} \quad \text{and} \quad W_{l,k}(\chi_R) = \frac{\omega_{l,k}}{ik\omega_R} e^{ik\chi_R}.$$

We can visualize the one-dimensional signal phase of Eq. (4) as a cross section along the line $t = \epsilon_u = \epsilon_m$ through a two-dimensional signal in a ϵ_u-ϵ_m coordinate system where the phase of this 2D signal would be given by

$$\Phi(\epsilon_u, \epsilon_m) = W_0 \epsilon_u + \sum_{l=1}^{L_{\max}} \sum_{\substack{k=-l \\ k\neq 0}}^{l} W_{l,k}(\chi_R) \left[e^{ik\omega_R \epsilon_m} - 1\right]. \qquad (5)$$

An important feature of this 2D signal is that it is periodic along the ϵ_m dimension according to

$$\Phi(\epsilon_u, \epsilon_m + nt_R) = \Phi(\epsilon_u, \epsilon_m), \qquad (6)$$

where n is an integer.

The significance of the ϵ_u-ϵ_m coordinate system is that only the rotor-modulated frequency contributions evolve along the ϵ_m dimension while only unmodulated frequency contributions evolve along the ϵ_u dimension. It was Dixon[6] who first showed that the two-dimensional signal phase in Eq. (5) can be obtained for arbitrary values of ϵ_u and ϵ_m by applying a series of π pulses carefully timed relative to the rotor phase after the excitation pulse. As described in the appendix, the timings for the π pulses are obtained from the simultaneous solution of a set of non-linear equations[6].

The signal phase in a PASS or MAT experiment is not measured along orthogonal dimensions of ϵ_u and ϵ_m, but rather in a 2D coordinate system that is related to the desired coordinate system by an affine transformation[16]. Both PASS and MAT can be implemented with five π pulses when $L_{\max} = 2$ with a sequence illustrated in Fig. 1A. While PASS and MAT solutions employing other than five π pulses exist[14], we consider only the five π pulse solutions without any loss of generality. In both PASS and MAT the five π pulses occur inside a constant time period T, which is an integer number of rotor periods (typically one rotor period), as shown in in Fig. 1A.

In the PASS experiment, the timings of the five π pulses are chosen so that at $t = 0$ the signal phase has the form

$$\Phi_{\mathrm{PASS}}(\epsilon_m, 0) = -\sum_{l=1}^{L_{\max}} \sum_{\substack{k=-l \\ k\neq 0}}^{l} W_{l,k}(\chi_R) \left[e^{ik\omega_R \epsilon_m} - 1\right] \qquad (7)$$

Notice that the PASS signal is designed so there is no unmodulated evolution phase during ϵ_m and that the rotor-modulated evolution phase during ϵ_m goes "backwards" leading to the refocusing of the modulated evolution into an echo during t along the line $t - \epsilon_m = 0$.

In the MAT experiment, the timings of the five π pulses are chosen so that at $t = 0$ the signal phase has the form

$$\Phi_{\mathrm{MAT}}(\epsilon_u, 0) = -W_0 \epsilon_u. \qquad (8)$$

The timings of the π pulses for the MAT experiment are designed so there is no rotor-modulated evolution phase during ϵ_u and the unmodulated evolution phase

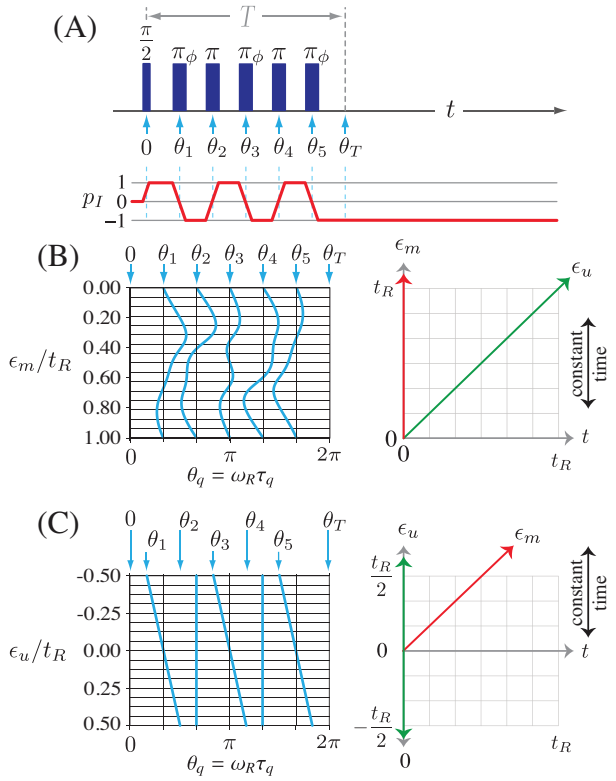

FIG. 1. (A) A generic five π pulse sequence when $L_{\max} = 2$ for both the PASS and MAT experiments along with p_I symmetry pathway[9]. The θ_j represent the rotor position $\theta_j = \omega_R t_j$ where t_j is the time from the initial excitation pulse. Instead of traditional phase cycling, the signal is acquired with a constant receiver phase while the phase of all π pulses with the ϕ subscript are incremented together into a single phase dimension[19]. (B) The π pulse timings for the PASS experiment along with symmetry pathways and the lines in the ϵ_m-t coordinates where the unmodulated and modulated evolutions refocus into echoes. (C) The π pulse timings for the MAT experiment along with symmetry pathways and the lines in the ϵ_u-t coordinates where the unmodulated and modulated evolutions refocus into echoes. In both (B) and (C) the direction of constant time relative to the initial excitation pulse is indicated.

goes "backwards" leading to the refocusing of the unmodulated evolution into an echo during t along the line $t - \epsilon_u = 0$.

Instead of traditional pulse phase cycling[22,23], the MAT or PASS signal can be acquired with a constant receiver phase while the phase of all π pulses having the ϕ subscripts shown in Fig. 1 are incremented together into a single phase dimension[19]. This results in a three-dimensional signal that is a function of ϵ, t, and ϕ. A Fourier transform of the 3D signal with respect to this pulse phase dimension yields the "accumulated" Δp spectrum from which the cross section at $\Delta p = -6$ contains the desired 2D MAT or PASS signal.

Both the MAT and PASS sequence of pulses can be modified for shifted-echo acquisition[24–26] by inserting n rotor periods before one of the preparatory π pulses as shown in Fig. 2. In shifted-echo acquisition the time origin is shifted into the acquisition window by nt_R. Shifted-echo acquisition can be advantageous, particularly for non-crystalline samples, where there is a strongly inhomogeneous broadening of resonances in the direct dimension.

B. PASS, TOP-PASS and TOP-MAT

The main advantage of PASS over MAT is that the signal in the indirect dimension, ϵ_m, is periodic with the rotor phase according to Eq. (6). For this reason, the PASS experiment only needs to sample the indirect dimension over a single rotor period. This is illustrated in the coordinate system at the far left of Fig. 3A. Here the grayscale rectangle represents the 2D PASS signal sampled over one rotor period in ϵ_m, and the grayscale transition from black to white represents the natural T_2 decay of the signal envelope. The symbol ϵ_u labels the line along which pure unmodulated evolution occurs, while the symbol ϵ_m labels the line along which pure rotor-modulated evolution occurs. Along the direct acquisition dimension, t, both rotor-modulated and unmodulated evolution occur. The direction of lines of constant time from the initial excitation pulse of the sequence are also indicated in this figure. An affine transformation can be applied to this signal to separate the pure rotor-modulated and unmodulated evolutions into orthogonal dimensions. One way to view the affine transformation of the 2D PASS signal is to imagine the digital sampling along the ϵ_m dimension as extending from $-\infty$ to $+\infty$. This can be easily achieved by translating copies of the acquired signal according to Eq. (6), as illustrated after the first step of Fig. 3A. From here the transformation can take one of two paths. Moving to the right is the conventional PASS transformation consisting of a single shear parallel to the ϵ_m axis and sheared towards negative values of ϵ_m, specified with a shear constant, $\kappa_{\epsilon_m} = -1$, and given by

$$\begin{bmatrix} t_m \\ t_u \end{bmatrix} = \underbrace{\begin{bmatrix} 1 & 0 \\ -1 & 1 \end{bmatrix}}_{\mathcal{K}_{\epsilon_m}} \begin{bmatrix} \epsilon_m \\ t \end{bmatrix}. \tag{9}$$

After the shear transformation the desired digital signal can be obtained by cropping out a 2D signal from one or more rotor periods of evolution along the ϵ_m dimension. Notice that the grayscale transition of the cropped 2D signal remains continuous and identical to the originally acquired signal.

In practice the acquired signal in conventional PASS processing is repeated only two or four times along the ϵ_m coordinate without any cropping of the final signal. While this signal repeat is not required it is done to give the appearance of separated spinning sidebands after the discrete Fourier transform.

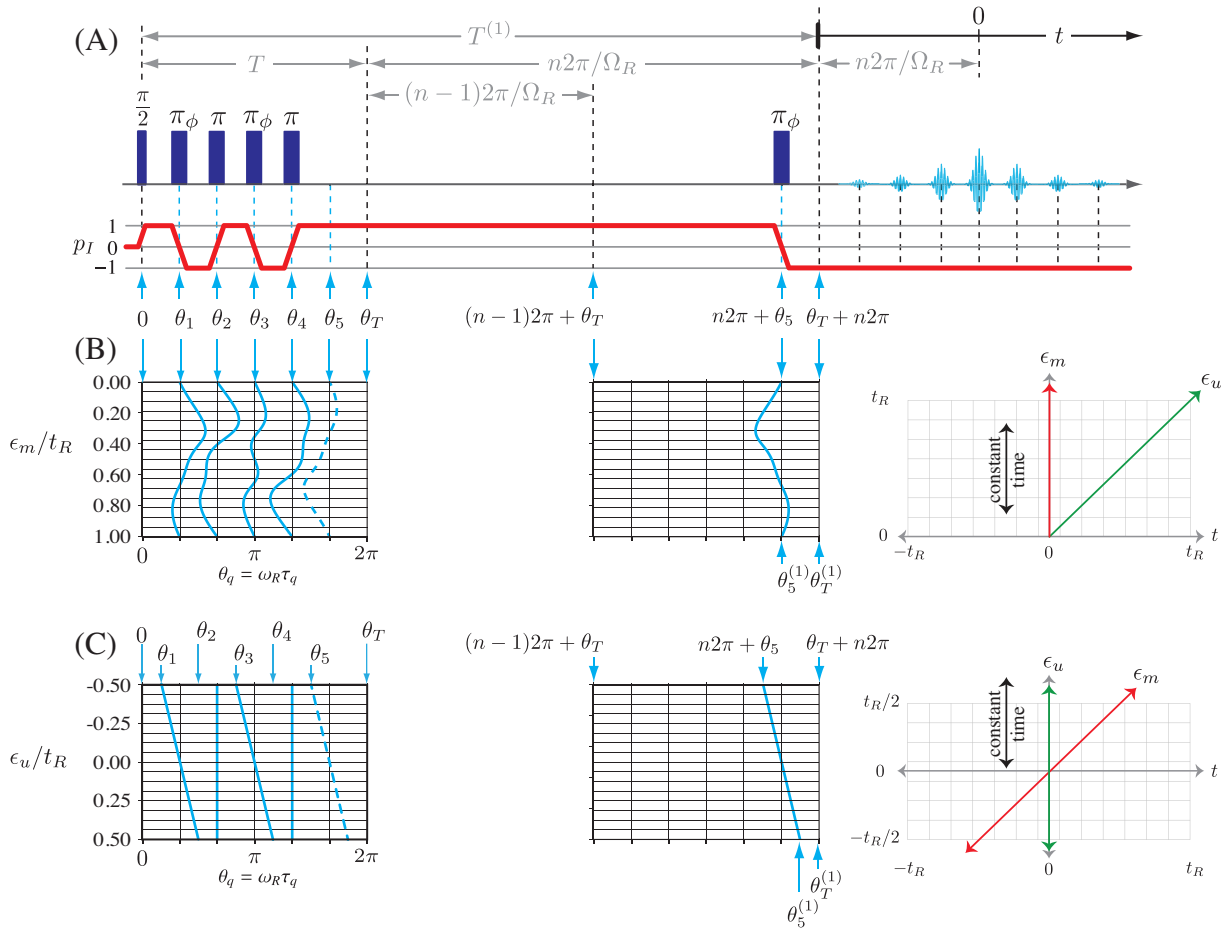

FIG. 2. (A) A generic five π pulse shifted-echo sequence $L_{\max}=2$ for PASS and MAT along with p_I symmetry pathway for samples with second-rank anisotropies. The θ_j values represent the rotor position $\theta_j=\omega_R t_j$ where t_j is the time from the initial excitation pulse. Instead of traditional phase cycling, the signal is acquired with a constant receiver phase while the phase of all π pulses with the ϕ subscript are incremented together into a single phase dimension[19]. (B) The π pulse timings for the PASS experiment and the lines in the ϵ_m-t coordinates where the unmodulated and modulated evolutions refocus into echoes. Below are the relevant effective symmetry pathways. (C) The π pulse timings for the MAT experiment and the lines in the ϵ_u-t coordinates where the unmodulated and modulated evolutions refocus into echoes. In both (B) and (C) the direction of constant time relative to the initial excitation pulse is indicated.

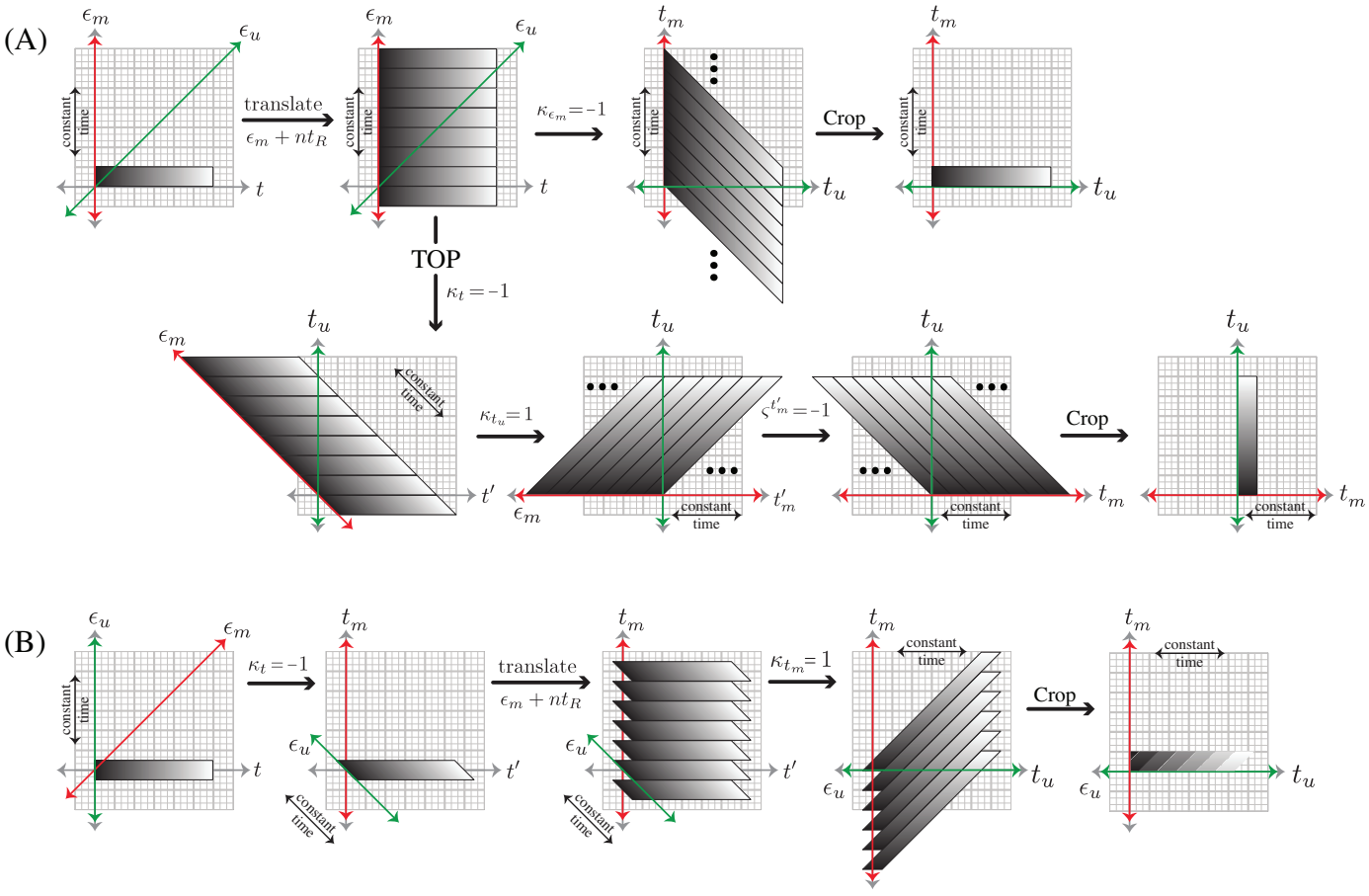

FIG. 3. Transformation of acquired signals, shown as grayscale-filled rectangle, into a 2D signal that correlates rotor-modulate evolution to unmodulated evolution. The gray scale gradient represents the signal envelope decay due to T_2 processes. The symbol ϵ_u labels the line along which pure unmodulated evolution occurs, while the symbol ϵ_m labels the line along which pure rotor-modulated evolution occurs. Along the direct acquisition dimension, t, both rotor-modulated and unmodulated evolution occur. The direction of lines of constant time from the initial excitation pulse of the sequence are also indicated. (A) Acquired PASS signal: In the first step, copies of acquired signal is translated according to Eq. (6). Moving from left to right above is the conventional PASS transformation consisting of a single shear parallel to the ϵ_m axis and sheared towards negative values of ϵ_m. Moving from left to right below is the TOP-PASS transformation consisting of a first shear that is parallel to the t dimension and sheared towards negative values of t. This shear is followed by a second shear parallel to the t_u dimension and sheared towards positive values of t_u. Finally a scaling is applied along the t'_m dimension. At the end of the conventional and TOP processing paths the desired digital signal is obtained by cropping out a 2D signal from one or more rotor periods of evolution along the ϵ_m dimension. The advantage of applying the TOP transformation to a PASS signal is that it can significantly reduce the number of samples required in the indirect dimension. (B) Acquired MAT signal: The affine transformation begins with a negative shear, $\mathcal{K}_t$, parallel to t, to create a 2D signal with unmodulated frequencies refocused along the vertical axis and the modulated frequencies refocused along $t' + \epsilon_m = 0$. Then a positive shear, $\mathcal{K}_{t_m}$, parallel to the vertical axis, t_m followed by a negative scaling, $\mathcal{S}_{t'_u}$, along t'_u. At the end of the processing paths the desired digital signal is obtained by cropping out a 2D signal from one or more rotor periods of evolution along the ϵ_m dimension.

In the context of NMR spectroscopy, Eq. (6) requires that additional care be taken when applying the discrete Fourier transform to the signal along the ϵ_m dimension. An underlying assumption behind the discrete Fourier transform is that the signal is periodic for all time with a period equal to the acquisition time. For a signal sampled for a full rotor period along ϵ_m this is indeed a correct assumption. For the majority of NMR signals, which are aperiodic, this is clearly not the case, and it is well known that the application of the discrete Fourier transform to an aperiodic signal introduces a baseline offset artifact. For this reason Otting et al.[27] introduced the procedure of dividing the amplitude of first point of the NMR signal by 2 to eliminate the baseline artifact which was the source of t_1 ridges in the early days of 2D NMR spectroscopy. Today, most NMR processing software automatically perform this divide by 2 correction before applying a discrete Fourier transform. However, if this correction is applied to a truly periodic signal, such as the signal along ϵ_m, then a baseline roll artifact will be introduced into the spectrum. Thus, special care must be taken to set the appropriate software flag so this correction is not performed when Fourier transforming along the ϵ_m coordinate, while still retaining this correction when Fourier transforming along the ϵ_u coordinate.

Recently, Davis et al.[16] introduced the TOP-PASS approach where the same double shear transformation as used in the Two-dimensional One Pulse (TOP) experiment[28,29] is applied to the PASS signal to swap the sampling intervals in the direct and indirect dimensions. This approach can significantly reduce the number of samples required in the indirect dimension. The TOP processing path, labeled in Fig 3A, consists of two shears and a scaling. The first shear is parallel to the t dimension and sheared towards negative values of t, specified with a shear constant, $\kappa_t = -1$. This shear is followed by a second shear parallel to the t_u dimension and sheared towards positive values of t_u, specified with a shear constant, $\kappa_{t_u} = 1$. Finally a scaling along the t'_m dimension with a scaling constant $\varsigma^{t'_m} = -1$ yields a 2D signal with rotor-modulated and unmodulated evolutions separated into orthogonal dimensions. The full transformation is given by[30]

$$\begin{aligned}\begin{bmatrix} t_m \\ t_u \end{bmatrix} &= \underbrace{\begin{bmatrix} 1 & 0 \\ 0 & -1 \end{bmatrix}}_{\mathcal{S}_{t'_m}} \underbrace{\begin{bmatrix} 1 & 1 \\ 0 & 1 \end{bmatrix}}_{\mathcal{K}_{t_u}} \underbrace{\begin{bmatrix} 1 & 0 \\ -1 & 1 \end{bmatrix}}_{\mathcal{K}_t} \begin{bmatrix} \epsilon_u \\ t \end{bmatrix}, \\ &= \begin{bmatrix} 0 & 1 \\ 1 & -1 \end{bmatrix} \begin{bmatrix} \epsilon_u \\ t \end{bmatrix}.\end{aligned} \tag{10}$$

After the TOP affine transformation, the desired digital signal can be obtained by cropping out a 2D signal from an integer number of rotor periods along the ϵ_m dimension. Again, notice that the grayscale transition of the cropped 2D signal remains continuous and identical to the originally acquired signal.

In practice, the TOP processing of a PASS signal requires the numerous signal repetitions along the ϵ_m coordinate unless special care is taken to set the direct dimension dwell time to an integer divisor of the rotor period, preferably an FFT compatible integer.

A disadvantage of MAT is that the indirect dimension, ϵ_u, needs to be sampled with an acquisition length that does not truncate the unmodulated evolution of the signal. This can be problematic since the indirect dimension in MAT is a constant time dimension[15]. Below we show that this problem can be overcome by applying the TOP processing approach of Davis et al.[16]. The MAT signal can be sampled over an indirect acquisition period from $-t_R/2$ to $t_R/2$, and then an affine transformation, as illustrated in Fig. 3B, is applied to separate the unmodulated and modulated frequency evolution into orthogonal dimensions. For the MAT signal this can be performed as a double shear, starting with a shear parallel to the t coordinate with a shear ratio of $\kappa_t = -1$, followed by a shear parallel to the t_m coordinate with a shear ratio of $\kappa_{t_m} = 1$, according to

$$\begin{aligned}\begin{bmatrix} t_m \\ t_u \end{bmatrix} &= \underbrace{\begin{bmatrix} 1 & 1 \\ 0 & 1 \end{bmatrix}}_{\mathcal{K}_{t_m}} \underbrace{\begin{bmatrix} 1 & 0 \\ -1 & 1 \end{bmatrix}}_{\mathcal{K}_t} \begin{bmatrix} \epsilon_u \\ t \end{bmatrix}, \\ &= \begin{bmatrix} 0 & 1 \\ -1 & 1 \end{bmatrix} \begin{bmatrix} \epsilon_u \\ t \end{bmatrix}.\end{aligned} \tag{11}$$

After this transformation the acquisition length along unmodulated evolution becomes that of the direct dimension. This transformation also leaves positive time for the unmodulated evolution dimension, ϵ_u, moving towards the left. Thus, an additional step in the processing would be to reverse the spectrum after the Fourier transform with respect to t_u.

In contrast to PASS, where the use of TOP processing is optional, TOP processing is required to eliminate the acquisition truncation artifact in nearly all MAT experiments. The exceptions being samples where significant inhomogenous broadenings act to dephase the signal completely during the constant time unmodulated evolution period. All further discussions of MAT will assume an indirect dimension sampled from $-t_R/2$ to $t_R/2$ followed by TOP processing.

As before, the desired digitized MAT signal can be obtained by cropping out a 2D signal from one or more rotor periods of evolution along the ϵ_m dimension. Unfortunately, as illustrated in Fig. 3B by the grayscale transition, the envelope of the cropped 2D signal contains a discontinuous T_2 dampening. These periodic discontinuities lead to artifacts in the unmodulated dimension that can become significant with decreasing T_2 relative to the rotor period. While the TOP processing eliminates the artifacts from truncated acquisition times, it introduces artifacts from the discontinuous T_2 dampening. This is a consequence of the lines of constant time from the initial excitation pulse not being parallel to the

pure rotor-modulated evolution, that is, the ϵ_m dimension. This artifact is also present in the recently introduced MAT-PASS experiment of Hung and Gan[17]. That experiment is essentially identical to TOP-MAT except that the first shear of the TOP transformation is performed through delayed acquisition in t by ϵ_m. This unavoidable discontinuous dampening artifact in the MAT experiment makes PASS is the preferred approach for separating rotor-modulated and unmodulated evolution.

In practice, however, whenever T_2 is significantly longer than a rotor period the discontinuous decay artifacts in MAT will be negligible. An experimental example of a 2D ^{13}C shielding correlation NMR spectrum of L-Histidine using the TOP-MAT approach is shown in Fig. 4. This spectrum appears identical to the TOP-PASS spectrum of Davis et al.[16]. This also confirms that MAT or PASS, when combined with TOP processing, can be used to generate the indirect dimension with a minimum sampling.

The modulated (sideband) cross sections along with best fit simulations are shown in Fig. 5. Each sideband pattern were fit using a C program employing the polycrystalline integration algorithm based on Lebedev quadrature over the unit sphere, as described by Eden and Levitt[31]. While anisotropic NMR lineshape analyses are often done in a non-linear least-square approach using the Levenberg-Marquardt algorithm[32], we have found that a modified bootstrap approach[32] employing a simplex algorithm gives more realistic parameter uncertainties. In the boot-strap approach the multi-dimensional statistical distribution of model parameters (intensity, δ_{xx}, and δ_{yy}) for each modulated cross-section is obtained after multiple least-squares analyses of sideband spectra generated by randomly choosing 32 sidebands with replacement from the experimental 32 sideband spectrum[32]. The mean model parameters with uncertainties using this approach are given in table I along with previously reported values by Strohmeier et al.[33].

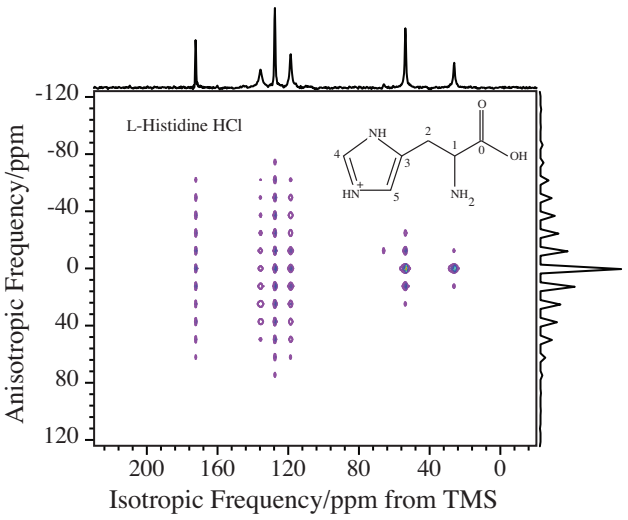

FIG. 4. Two-dimensional MAT spectrum of L-Histidine along with one-dimensional projections. The 2D spectrum was obtained using double shear (TOP) processing[16]. Isotropic frequencies are referenced to TMS. Contour levels are plotted from 5%-100% in increments of 5% of the maximum intensity.

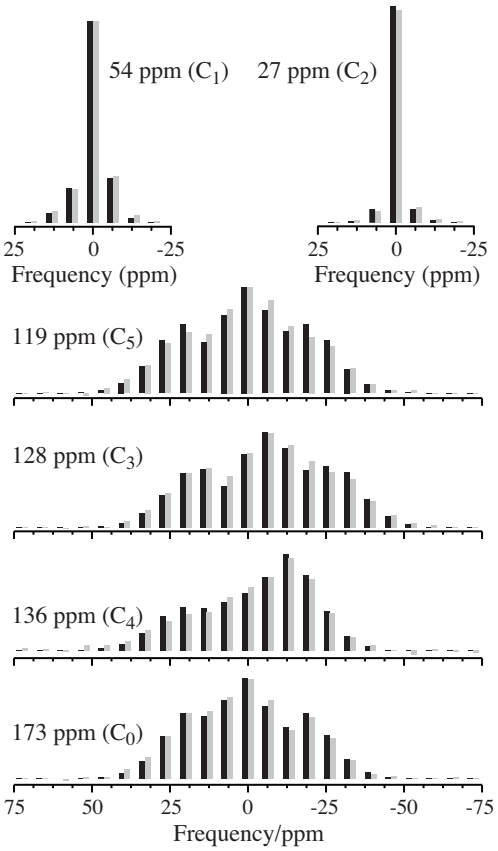

FIG. 5. Rotor modulated cross sections of the L-Histidine TOP-MAT spectrum shown in Fig. 4 along with best-fit simulations for each site. Experimental sideband amplitudes are shown as gray bars while best fit simulations are shown as black bars.

C. TOP-MAT and PASS with Echo Train Acquisition

Echo train acquisition can be appended to both TOP-MAT and PASS by using the shifted-echo sequence of Fig. 2 as a starting point. All acquired echoes will be valid MAT or PASS echoes *provided the train of echo-refocusing π pulses*, shown as open rectangles in Fig. 6, *are equally spaced and positioned at times where the sum of the indirect and direct rotor modulated evolution phase is an integer multiple of* 2π. This is achieved by inserting a delay of ϵ_m before the echo train acquisition, as shown in Fig. 6.

In the case of TOP-MAT, where only unmodulated frequency evolution occurs in the indirect dimension, i.e., $\epsilon_m = 0$, the train of echo-refocusing π pulse po-

	$\delta_{\rm iso}$/ppm	δ_{xx}/ppm		δ_{yy}/ppm		δ_{zz}/ppm	
Site		This work	Ref. 33	This work	Ref. 33	This work	Ref. 33
C_0	173.0 ± 2.0	171.3 ± 1.8	-	107.7 ± 1.8	-	239.8 ± 1.8	-
C_1	54.0 ± 2.0	57.8 ± 3.8	57.0	69.1 ± 2.1	68.5	35.1 ± 2.6	37.8
C_2	27.0 ± 2.0	26.8 ± 4.0	-	37.3 ± 2.8	-	16.8 ± 2.2	-
C_3	127.0 ± 2.0	200.3 ± 2.1	198.2	131.6 ± 2.4	132.3	52.0 ± 1.8	49.8
C_4	136.0 ± 2.0	157.8 ± 3.8	-	196.9 ± 3.4	-	53.3 ± 3.4	-
C_5	119.0 ± 2.0	121.0 ± 2.6	122.8	187.5 ± 3.0	190.4	48.4 ± 2.8	44.3

TABLE I. Best fit values of the isotropic shift and principal components of the chemical shift tensor for L-Histidine. All uncertainties are one standard deviation. Also shown, for comparison, are the values obtained by Strohmeier et. al[33].

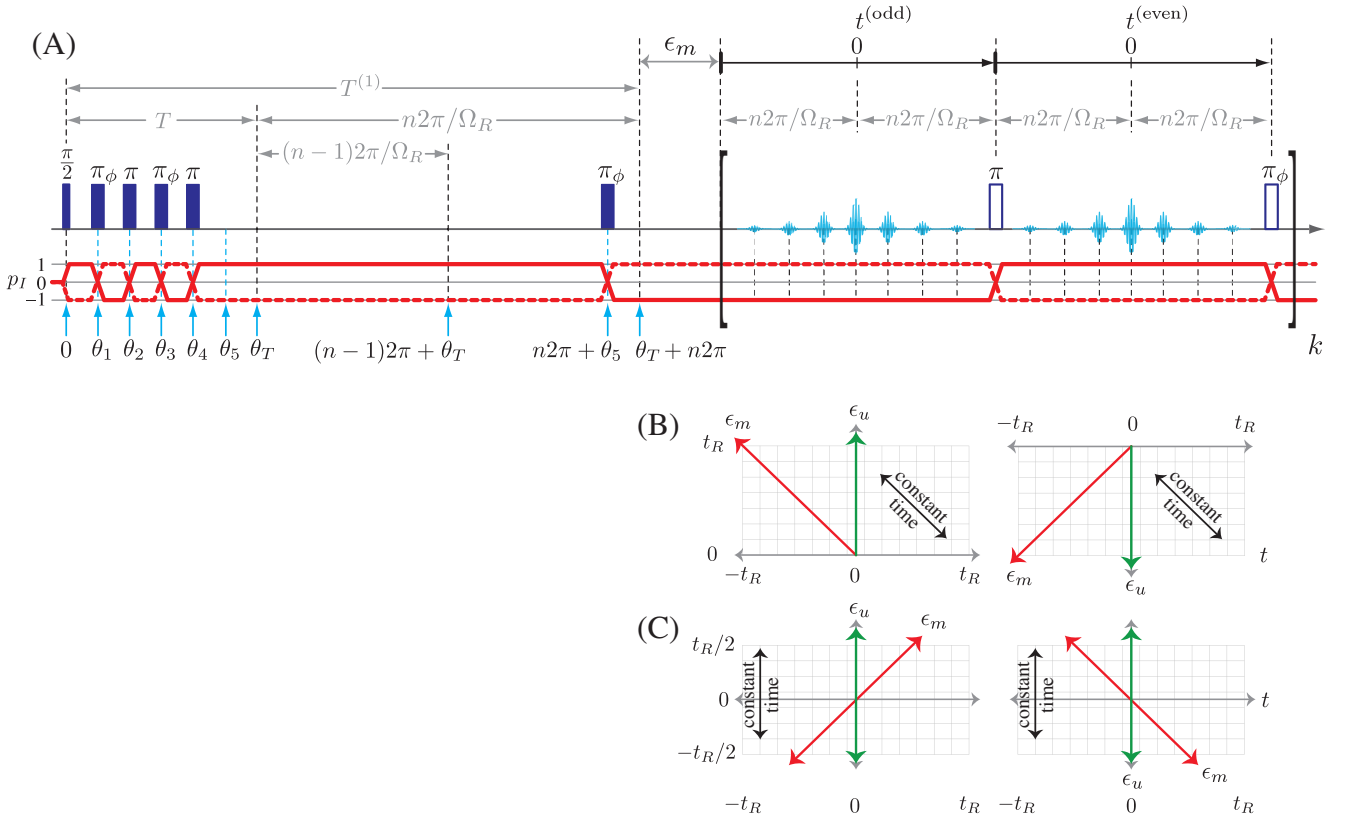

FIG. 6. (A) Five π pulse sequence for TOP-PASS or TOP-MAT with PIETA along with p_I symmetry pathways. Instead of traditional phase cycling, the signal is acquired with a constant receiver phase while the phase of all π pulses with the ϕ subscript are incremented together into a PIETA phase dimension[19]. The θ_j values represent the rotor position $\theta_j = \omega_R t_j$ where t_j is the time from the initial excitation pulse. The PIETA π pulses, shown as unfilled rectangles, must be shifted forward by ϵ_m. In PASS the values of ϵ_m depend on the timings of the initial five π pulses as illustrated in Fig. 1. In TOP-MAT the value of $\epsilon_m = 0$ for all timings of the initial five π pulses, that is, all echo train acquisition pulses remain at a fixed time from the initial excitation pulse. (B) The lines where the unmodulated and modulated interactions refocus in the ϵ_u-t coordinates for even and odd echoes in the PASS experiment. (C) The lines where the unmodulated and modulated interactions refocus in the ϵ_u-t coordinates for even and odd echoes in the MAT experiment.

sitions remain constant relative to the first excitation pulse, i.e., not shifting with changing ϵ_u. This set of timings matches the MAT-CPMG sequence described by Hung et. al.[18]. As shown in Fig. 6C, the unmodulated frequency evolution during ϵ_u refocuses into an echo in the middle of each direct dimension of the echo train. The modulated frequency evolution refocuses along the line $t^{(odd)} - \epsilon_u = 0$ in odd echoes and along the line $t^{(even)} + \epsilon_u = 0$ in even echoes of the train. While the odd echoes are processed in the same double shearing transformation shown in Fig. 3B, the even echoes must be processed with opposite signs for the two shearing factors using the double shearing transformation shown in Fig. 3B. Both even and odd echoes can then be combined in a matched filter[34] to obtain full sensitivity enhancement from echo train acquisition. It is important to note in Fig. 6C that with increasing ϵ_m the lines of pure rotor-modulated evolution in both the even and odd echoes are not parallel to the lines of constant time. Thus, after the necessary affine transformation both even and odd signals will suffer from the same discontinuous T_2 dampening seen in the TOP-MAT experiment.

In the case of PASS, where modulated frequency evolution occurs in the indirect dimension, the train of echo-refocusing π pulses, shown as open rectangles in Fig. 6, must be shifted forward by ϵ_m. As shown in Fig. 6B, the addition of the ϵ_m shift causes the unmodulated frequency evolution to refocus into an echo in the middle of each direct dimension of the echo train. Similarly, the ϵ_m shift leads to the unmodulated frequency evolution refocusing along the line $t^{(odd)} + \epsilon_u = 0$ in odd echoes and along the line $t^{(even)} - \epsilon_u = 0$ in even echoes of the train. Because of the delayed acquisition, the affine transformation that is applied to the odd MAT-PIETA echoes must also be applied to the even PASS-PIETA echoes and vice versa. Also note in Fig. 6B that with increasing ϵ_m the lines of pure rotor-modulated evolution in the odd echoes are parallel to the lines of constant time. Therefore, the signal from the odd echoes will not suffer from the discontinuous T_2 dampening artifact seen in the TOP-MAT experiment. For the even echoes, however, the lines of pure rotor-modulated evolution increasing ϵ_m are not parallel to the lines of constant time. Thus, the even echoes suffer from the same discontinuous T_2 dampening seen in the TOP-MAT experiment. In fact, the lines of pure rotor-modulated evolution in the even echoes move away from the constant time line at twice the rate as the even and odd echoes in the MAT-PIETA experiment. So, the even echoes in PASS-PIETA will have stronger discontinuities in the T_2 dampening of its envelope along the pure unmodulated evolution dimension. In practice, since echo train acquisition is most advantageous when T_2 is long compared to the π pulse spacing, the discontinuous T_2 dampening artifact in even and odd MAT-PIETA echoes and the even PASS-PIETA echoes will likely be negligible. Of course, the odd-echo PASS-PIETA will always be without such artifacts and can be readily used to verify the validity of the even-echo PASS-PIETA signal.

One might think that the echo train acquisition approach of Carr-Purcell-Meiboom-Gill (CPMG)[35,36] can be easily appended to a sequence like MAT or PASS to obtain enhanced sensitivity. This approach, however, is not trivial for any phase modulated signal exiting the mixing period. Using CPMG on a phase modulated signal like MAT or PASS would introduce a spectral artifact due to undesired coherence transfer pathways[19]. One simple solution for CPMG acquisition is to convert phase modulated coherence into amplitude modulation via a z-filter before conversion into observable coherence, but this comes with a loss in sensitivity. Gan and coworkers[18] showed that CPMG can be appended to MAT by employing a rather complicated phase cycle with multiplex acquisition scheme. Here we present a simpler alternative: Phase Incremented Echo Train Acquisition (PIETA)[19]. In this approach the phase of every other refocusing pulse, ϕ, is incremented as a single variable, creating an additional phase dimension. The receiver phase is held constant in PIETA, avoiding cumbersome or intractable phase cycling schemes where the receiver phase must follow a master equation[22,23]. A Fourier transform with respect to the PIETA phase, ϕ, converts the ϕ dimension into a Δp dimension where desired signals are easily separated from undesired coherence transfer pathway signals. This is illustrated in Fig. 7 for the ^{29}Si TOP-MAT-PIETA experiment on a Cu(II)-doped mixed potassium/magnesium tetrasilicate glass. As acquired, this is a four-dimensional experiment, depending on ϵ_{u}, t, ϕ, and n (echo count). Figure 7 only shows a magnitude-mode cross-section through the origin of ϵ_{u} and t. The general idea in PIETA is to collectively increment the phases of selected pulses so the desired pathway signals fall along the extremities of a sideways "V" pattern with undesired pathway signals appearing inside the sideways "V". In the case of TOP-MAT and PASS the π pulses in the preparation period are included in the PIETA phase increment so the desired signal in the first odd echo appears at $\Delta p = -6$ and desired signal in the first even echo the appears at $\Delta p = 6$. The positions of the desired signals in TOP-MAT-PIETA and TOP-PASS-PIETA as a function of echo count are given by

$$\Delta p(n) = (-1)^n \left\{ 2 \left\lfloor \frac{n-1}{2} \right\rfloor + 6 \right\}, \qquad (12)$$

where $\lfloor x \rfloor$ represents the integer part or floor function of x. The desired even and odd echoes taken along Eq. (12) can be separated and both reduced down in a weighted average to maximize sensitivity[34] into even and odd 2D signals as a function of ϵ_u and t. The resulting signal can then be processed as one would have without PIETA. That is, even and odd 2D signals are each processed using the TOP approach as described above, and finally combined into the final 2D TOP-MAT-PIETA spectrum correlating modulated and unmodulated evolution spectra shown in Fig. 8B. For comparison, the 2D TOP-MAT of the same sample is shown in Fig. 8A, demonstrating a PIETA sensitivity enhancement of 2.70.

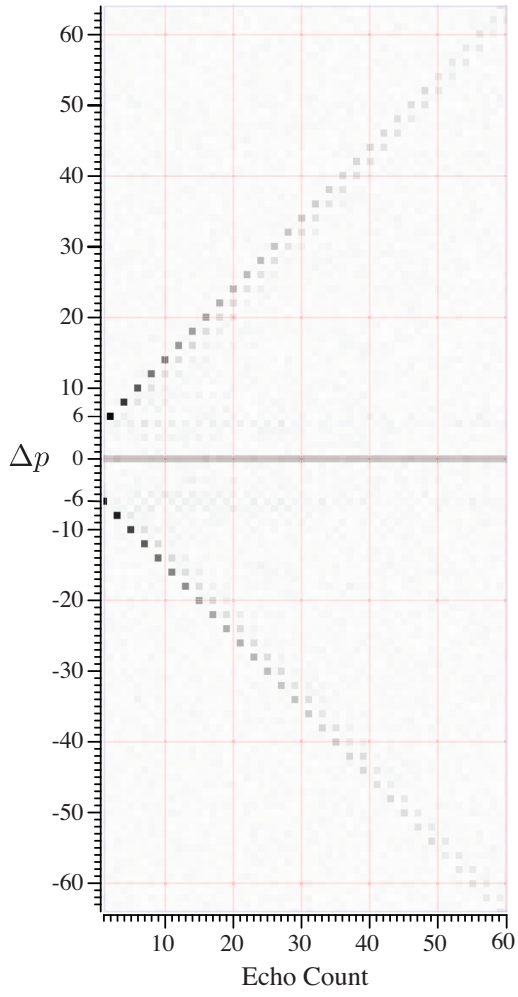

FIG. 7. Experimental 2D PIETA cross sections taken through the time origin of a ^{29}Si TOP-MAT-PIETA experiment on a Cu(II)-doped mixed potassium/magnesium tetrasilicate glass. The Δp range from -64 to +64 was obtained using $\Delta\phi_P = 2\pi/128$. Sixty PIETA echoes were acquired.

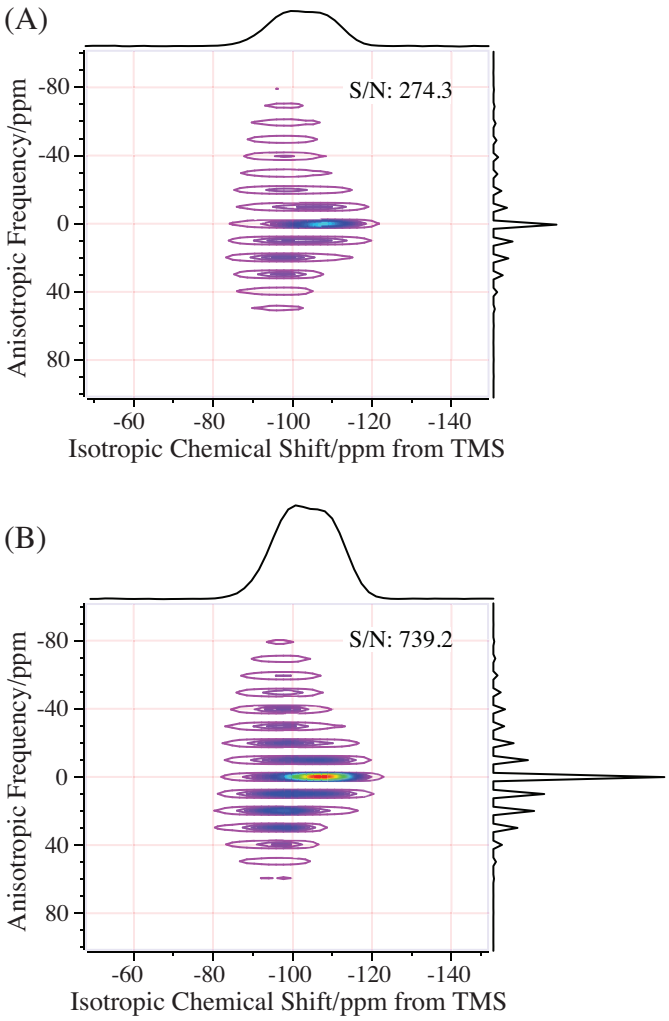

FIG. 8. Comparison of the TOP-MAT spectra of a Cu(II)-doped mixed potassium/magnesium tetrasilicate glass in which A) a single shifted echo was acquired and B) TOP-MAT-PIETA was used to acquire sixty echoes. All echoes were individually matched and coadded to produce the result. This procedure yields a MAT spectrum with a signal-to-noise ratio that is a factor 2.70 higher than the shifted echo experiment, with only a 1.5% increase of experiment time due to acquisition of multiple echoes.

In this tetrasilicate glass composition the ^{29}Si resonances arise from polymerized SiO_4 tetrahedra whose chemical shift anisotropy is related to the degree of connectivity of the tetrahedron to the network. Specifically, there are two types of environments in this glass composition: fully connected SiO_4 tetrahedra, $Q^{(4)}$ sites, having little to no anisotropy, and $Q^{(3)}$ sites, where only three oxygen are interconnecting, having a significant axially symmetric anisotropy[37–40]. From the changing width of the spinning sideband patterns in Fig. 8 it appears that the $Q^{(4)}$ sites fall in the region of isotropic chemical shifts from -120 ppm to -100 ppm while the $Q^{(3)}$ sites appear in the region from -100 ppm to -80 ppm. In a more detailed analysis of this ^{29}Si TOP-MAT-PIETA spectrum the statistical distribution of $Q^{(n)}$ can be determined. This spectrum along with ^{29}Si TOP-MAT-PIETA spectra of a series of other glasses with similar compositions will be analyzed and published elsewhere.

1. TOP-QMAT-PIETA

The ideas presented here can also be extended to the second-order broadened central transition of half-integer $I > \frac{1}{2}$ nuclei. When the electric quadrupole coupling of a nucleus is no longer negligible compared to the Zeeman coupling there will be second-order and possibly higher-order contributions to the NMR frequency. Using the notation of symmetry pathways[9], the second-order con-

tribution to NMR frequency is given by

$$\Omega_q^{(2)}(\Theta, m_i, m_j) = \frac{\omega_q^2}{\omega_0}\left[\mathbb{S}^{\{qq\}} \cdot \mathbb{c}_0(m_i, m_j)\right] + \frac{\omega_q^2}{\omega_0}\left[\mathbb{D}^{\{qq\}}(\Theta) \cdot \mathbb{c}_2(m_i, m_j)\right] + \frac{\omega_q^2}{\omega_0}\left[\mathbb{G}^{\{qq\}}(\Theta) \cdot \mathbb{c}_4(m_i, m_j)\right]. \quad (13)$$

Here $\mathbb{c}_0(m_i, m_j)$, $\mathbb{c}_2(m_i, m_j)$, and $\mathbb{c}_4(m_i, m_j)$ are spin transition symmetry functions, which are tabulated for various nuclear spin angular momenta, I, in Ref. 9, and $\mathbb{S}$, $\mathbb{D}(\Theta)$, and $\mathbb{G}(\Theta)$ represent the zero-, second-, and fourth-rank spatial symmetry functions[9]. Additionally, Θ is the Euler angle specifying the orientation of sample in the laboratory frame, ω_0 is the Larmor frequency, and ω_q is the quadrupolar splitting given by

$$\omega_q = \frac{6\pi C_q}{2I(2I-1)}, \quad (14)$$

where C_q is the quadrupole coupling constant.

Under sample rotation one can show that Eq. (13) takes the form of Eq. (1) with values of $L = 0$, 2, and 4. With $L_{\max} = 4$, the MAT and PASS π timing solutions (see appendix) typically have nine π pulses[41]. Massiot and coworkers[21] introduced the QPASS experiment and Gan and coworkers[20] introduced the QMAT experiment for separating sidebands of the central transition of half-integer quadrupolar nuclei.

All the principles from the previous sections can be adapted in the design of the TOP-QMAT-PIETA and QPASS-PIETA experiments by simply using nine π pulses instead of five in the constant time preparation period of the sequence in Fig. 6A. With the increase from five to nine π pulses the positions of the desired signals in TOP-MAT-PIETA and TOP-PASS-PIETA as a function of echo count are given by

$$\Delta p(n) = (-1)^n \left\{2\left\lfloor\frac{n-1}{2}\right\rfloor + 10\right\}. \quad (15)$$

An experimental illustration of a ^{87}Rb TOP-QMAT-PIETA experiment on polycrystalline Rb_2SO_4 is shown in Fig. 9. Because MAS cannot fully average away the 4th-rank spatial anisotropy of second-order quadrupole broadening the projection on the unmodulated frequency dimension does not yield an isotropic spectrum. Instead, it only provides the infinite speed MAS spectrum. Since multiple sites have overlapping anisotropic resonances in the unmodulated frequency dimension the cross-sections taken parallel to the modulated frequency (sideband order) dimension, mix sideband contributions from overlapping resonances. Thus, the value of QMAT and QPASS is primarily in the projection onto the infinite speed dimension and the value of PIETA acquisition comes when transverse relaxation times are long enough to provide a significant sensitivity advantage. Clearly, the main application of QMAT or QPASS is eliminating spinning sidebands when the MAS speeds are insufficient. In such situations, however, the nutation frequency can be less than the anisotropic linewidth. Thus, resonance offset effects, which accumulate through the nine π pulses of QMAT or QPASS, can result in lineshape distortions in the "infinite speed" projection. That is, spectral intensities at larger resonance offsets can get reduced, although the positions of singularities in the powder pattern lineshape generally remain unchanged.

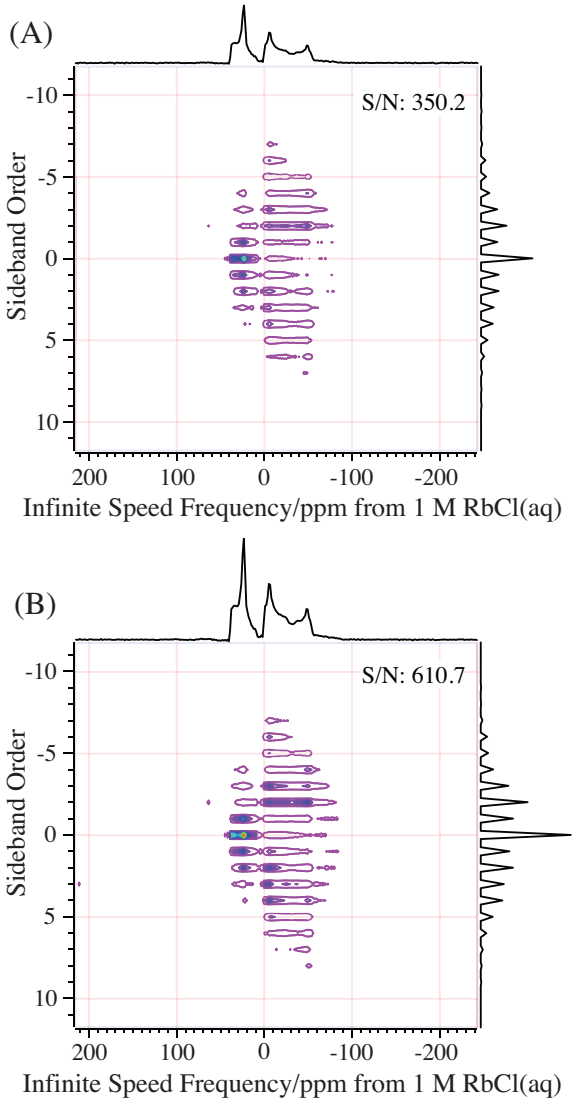

FIG. 9. Comparison of (A) shifted-echo TOP-QMAT and (B) TOP-QMAT-PIETA spectra of $^{87}Rb_2SO_4$. PIETA was used to acquire 22 echoes, which were individually matched and coadded to produce the result. This procedure yields a QMAT spectrum with a signal-to-noise ratio that is a factor of 1.74 greater than that of the shifted echo experiment, with a 15.7% increase in experiment time.

IV. SUMMARY

We have attempted to present a more intuitive picture of how time evolution arising from rotor modulated contributions to the NMR transition frequency can be separated from unmodulated contributions by viewing MAT and PASS experiments in coordinate systems that are related through affine transformations.

We have shown that a simple post-acquisition processing algorithm involving a double shear affine transformation, as used in processing signals from the TOP experiment[16,29], can be used not only to reduce the number of measurements needed in the indirect dimension of the MAT experiment but can also eliminate truncated acquisition time artifacts. This solution, however, comes at the cost of introducing an artifact of discontinuous T_2 dampening of the signal along the unmodulated evolution dimension. While TOP, PASS and TOP-PASS avoid both of these artifacts, we found no solution for eliminating the discontinuous T_2 dampening artifact from MAT.

In situations where there is a homogenous distribution of unmodulated frequencies, as in the isotropic shifts of non-crystalline solids or the residual anisotropic shifts in the central transition of quadrupole nuclei, the addition of echo train acquisition to MAT or PASS can provide significant sensitivity gains. While the addition of echo train acquisition to MAT is relatively straightforward, the addition to PASS requires an understanding that the refocusing π pulses must be equally spaced and positioned at times where the total rotor modulated evolution phase is an integer multiple of 2π. Thus, echo train acquisition can be added to PASS simply by shifting the train of refocusing pulses by the indirect evolution time. Magic-Angle Turning with echo train acquisition still remains tainted by discontinuous T_2 dampening along the unmodulated evolution dimension. While the T_2 dampening of unmodulated evolution dimension in the odd echoes of PASS remains continuous, the even echoes of PASS suffer from the same discontinuous T_2 dampening seen in the MAT experiment.

Generally, echo train acquisition cannot be added to NMR pulse sequences with a phase modulated signal exiting the mixing period, like MAT or PASS, without taking special precautions to prevent artifact signals from undesired coherence transfer pathways from contaminating the signal. We have presented a robust approach with a straightforward implementation, called PIETA, which eliminates these artifacts with only the cost of additional post-acquisition signal processing.

Combining these ideas together we demonstrate enhanced sensitivity with a TOP-MAT-PIETA sequence on ^{29}Si NMR of a silicate glass where different silicate tetrahedra environments can be distinguished by distinctly different spinning sideband patterns. Likewise, we adapt these approaches in the TOP-QMAT-PIETA experiment, which provides an "infinite speed" MAS spectrum of the central transition of half-integer quadrupolar nuclei, to provide enhanced sensitivity.

Although these ideas were initially developed in the field solid-state NMR they are also applicable in the realm of magnetic resonance imaging of rotating samples[3,4] including recent work by Sakellariou and coworkers[5].

ACKNOWLEDGMENTS

This material is based upon work supported by the National Science Foundation under Grant No. NSF CHE-1012175. The authors would like to thank Eric Keeler for synthesis of the $KMg_{0.5}O_2 \cdot 4SiO_2$ glass, and Michael Davis for helpful discussions during the early stages of this work.

Appendix A: MAT and PASS Timing Solutions

The NMR signal in a rotating sample can be manipulated into a number of desirable forms by applying a series of π pulses between the initial excitation pulse and the start of signal acquisition. In the PASS and MAT experiments[6,13], a time coordinate is defined where the initial excitation pulse is applied at $t = -T$ and signal acquisition begins at $t = 0$. Between the initial excitation pulse and signal acquisition are Q π-pulses, applied at times $-T+\tau_1, -T+\tau_2, \ldots, -T+\tau_Q$. The signal phase at $t = 0$, a duration of $\tau_{Q+1} = T$ after the initial excitation pulse, is given by

$$\begin{aligned}\Phi_Q(t=0) &= (-1)^Q \sum_{q=0}^{Q}(-1)^q \int_{-T+\tau_q}^{-T+\tau_{q+1}} \Omega(t')dt', \\ &= W_0 \left[T - 2(-1)^Q \sum_{q=1}^{Q}(-1)^q \tau_q\right] \\ &+ \sum_{l=1}^{L_{\max}} \sum_{\substack{k=-l \\ k\neq 0}}^{l} W_{l,k}(\chi_R) \\ &\times \left[1 - 2(-1)^Q \sum_{q=1}^{Q}(-1)^q e^{im\theta_q} e^{-im\theta_T} - (-1)^Q e^{-im\theta_T}\right],\end{aligned} \tag{A1}$$

where $\tau_0 = 0$, $\theta_T = \omega_R T$, $\theta_q = \omega_R \tau_q$, and $L_{\max}$ is the rank of the highest spatial tensor contributing to the NMR transition frequency. We constrain the initial rotor phase, χ_R, to be identical in every PASS or MAT experiment. In polycrystalline samples, however, this constraint is unnecessary[42].

1. PASS

In the PASS experiment[6,43] the timings of the Q π pulses are manipulated so the signal phase at $t = 0$ has

a form

$$\Phi_{\rm pass}(\epsilon_m, t=0) = W_0 \cdot [\ 0\ ] - \sum_{l=1}^{L_{\rm max}} \sum_{\substack{k=-l \\ k\neq 0}}^{l} W_{l,k}(\chi_R)\left[e^{ik\omega_R\epsilon_m} - 1\right], \quad \text{(A2)}$$

where ϵ_m is a function of the Q π pulse timings. Evolving forward from $t = 0$ the PASS signal phase then becomes similar to the Bloch decay MAS signal

$$\Phi_{\rm pass}(\epsilon_m, t) = W_0\ t + \sum_{l=1}^{L_{\rm max}} \sum_{\substack{k=-l \\ k\neq 0}}^{l} W_{l,k}(\chi_R)\left[e^{ik\omega_R t} - e^{ik\omega_R\epsilon_m}\right], \quad \text{(A3)}$$

with the important exception that ϵ_m is non-zero and can be varied independent of t. From the last term in square brackets in Eq. (A9) it is clear that the modulated frequency contribution refocuses during t when $t - \epsilon_m = 0$.

The π pulse timings for the PASS experiment come from equating Eqs. (A1) and (A2) to obtain the Dixon equations:

$$\theta_T - 2(-1)^Q \sum_{q=1}^{Q} (-1)^q \theta_q = 0, \quad \text{(A4)}$$

and

$$e^{im\Theta_m} = 2(-1)^Q \sum_{q=1}^{Q} (-1)^q e^{im\theta_q} e^{-im\theta_T} + (-1)^Q e^{-im\theta_T}, \quad \text{(A5)}$$

where $\Theta_m = \omega_R\epsilon_m$. Levitt and coworkers[13] suggested a 2D PASS experiment of constant duration T with $\theta_T = 2\pi$ and obtained the equations

$$2\sum_{q=1}^{Q} (-1)^q \theta_q + 2\pi = 0, \quad \text{(A6)}$$

and

$$-2\sum_{q=1}^{Q} (-1)^q e^{ik\theta_q} - 1 = e^{ik\Theta_m}, \quad \text{for } k = 1, \ldots, L_{\rm max}. \quad \text{(A7)}$$

These equations can be solved numerically in the case where $L_{\rm max} = 2$ for the five π pulse timings shown in Fig. 1 and tabulated elsewhere[13].

2. MAT

In the MAT experiment the timings of the Q π pulses are manipulated so the signal phase at $t = 0$ has a form

$$\Phi_{\rm MAT}(\epsilon_u, t=0) = -W_0\epsilon_u, \quad \text{(A8)}$$

where ϵ_u is a function of the Q π pulse timings.

Evolving forward from $t = 0$ the MAT signal phase then becomes similar to the Bloch decay MAS signal

$$\Phi_{\rm MAT}(\epsilon_u, t) = W_0\ (t - \epsilon_u) + \sum_{l=1}^{L_{\rm max}} \sum_{\substack{k=-l \\ k\neq 0}}^{l} W_{l,k}(\chi_R)\left[e^{ik\omega_R t} - 1\right], \quad \text{(A9)}$$

with the important exception that ϵ_u is non-zero and can be varied independent of t. From the last term in square brackets in Eq. (A9) it is clear that the unmodulated frequency contribution refocuses during t when $t - \epsilon_u = 0$.

The π pulse timings for the MAT experiment come from equating Eqs. (A1) and (A8) to obtain the equations:

$$\theta_T - 2(-1)^Q \sum_{q=1}^{Q} (-1)^q \theta_q = \Theta_u, \quad \text{(A10)}$$

and

$$2(-1)^Q \sum_{q=1}^{Q} (-1)^q e^{im\theta_q} e^{-ik\theta_T} - (-1)^Q e^{-ik\theta_T} = 1, \quad \text{(A11)}$$

where $\Theta_u = \omega_R\epsilon_u$. A 2D MAT experiment, of constant duration T with $\theta_T = 2\pi$, leads to the equations

$$2\sum_{q=1}^{Q} (-1)^q \theta_q + 2\pi = \Theta_u, \quad \text{(A12)}$$

and

$$\sum_{q=1}^{Q} (-1)^q e^{ik\theta_q} = 0, \quad \text{for } k = 1, \ldots, L_{\rm max}. \quad \text{(A13)}$$

Analytic solutions for this problem can be derived based upon symmetry arguments[14]. A solution with $Q = 2L_{\rm max} + 1$ is given by

$$\theta_q = \frac{\pi}{L_{\rm max} + 1}\left[q + [1 - (-1)^q]\,\frac{\Theta_u}{4\pi}\right]. \quad \text{(A14)}$$

In this solution the π pulses associated with even q are stationary in time and equally spaced at integer multiples of $t_R/(L_{\rm max} + 1)$, whereas the π pulses associated with odd q have timings that increase linearly with ϵ_u and occur precisely at the midpoint of the interval between neighboring even q pulses when $\epsilon_u = 0$.

[1] G. A. Williams and H. S. Gutowsky, Phys. Rev. **104**, 278 (1956).
[2] M. M. Maricq and J. S. Waugh, J. Chem. Phys. **70**, 3300 (1979).
[3] Y. Ogura and K. Sekihara, J. Magn. Reson. **92**, 490 (1990).
[4] J. H. Baltisberger, S. Hediger, and L. Emsley, J. Magn. Reson. **172**, 79 (2005).
[5] A. Wong and D. Sakellariou, Chem. Phys. Chem. **12**, 3529 (2011).
[6] W. T. Dixon, J. Chem. Phys. **77**, 1800 (1982).
[7] N. M. Szeverenyi, A. Bax, and G. E. Maciel, J. Magn. Reson. **61**, 440 (1984).

[8] A. Samoson, B. Q. Sun, and A. Pines, "New angles in motional averaging," in *Pulsed Magnetic Resonance: NMR, ESR, and Optics - A recognition of E. L. Hahn* (Clarendon Press, Oxford, 1992) pp. 80–94.
[9] P. J. Grandinetti, J. T. Ash, and N. M. Trease, Prog. N.M.R. Spect. **59**, 121 (2011).
[10] Z. H. Gan, J. Am. Chem. Soc. **114**, 8307 (1992).
[11] J. Z. Hu, D. W. Alderman, C. H. Ye, R. J. Pugmire, and D. M. Grant, J. Magn. Reson. A **105**, 82 (1993).
[12] S. L. Gann, J. H. Baltisberger, and A. Pines, Chem. Phys. Lett. **210**, 405 (1993).
[13] O. N. Antzutkin, S. C. Shekar, and M. H. Levitt, J. Magn. Reson. A **115**, 7 (1995).
[14] O. N. Antzutkin, Prog. NMR Spect. **35**, 203 (1999).
[15] D. W. Alderman, G. McGeorge, J. Z. Hu, R. J. Pugmire, and D. M. Grant, Molec. Physics **95**, 1113 (1998).
[16] M. Davis, K. M. Shookman, J. D. Sillaman, and P. J. Grandinetti, J. Magn. Reson **210**, 51 (2011).
[17] I. Hung and Z. H. Gan, J. Magn. Reson. **204**, 150 (2010).
[18] I. Hung, T. Edwards, S. Sen, and Z. H. Gan, J. Magn. Reson. **221**, 103 (2012).
[19] J. H. Baltisberger, B. J. Walder, E. G. Keeler, D. C. Kaseman, K. J. Sanders, and P. J. Grandinetti, J. Chem. Phys. **136**, 211104 (2012).
[20] I. Hung and Z. H. Gan, Chem. Phys. Lett. **496**, 162 (2010).
[21] D. Massiot, V. Montouillout, F. Fayon, P. Florian, and C. Bessada, Chem. Phys. Lett. **272**, 295 (1997).
[22] G. Bodenhausen, H. Kogler, and R. R. Ernst, J. Magn. Reson. **58**, 370 (1984).
[23] A. D. Bain, J. Magn. Reson. **56**, 418 (1984).
[24] P. J. Grandinetti, J. H. Baltisberger, A. Llor, Y. K. Lee, U. Werner, M. A. Eastman, and A. Pines, J. Magn. Reson. A **103**, 72 (1993).
[25] F. Fayon, C. Bessada, A. Douy, and D. Massiot, J. Magn. Reson. **137**, 116 (1999).
[26] F. G. Vogt, J. M. Gibson, D. J. Aurentz, K. T. Mueller, and A. J. Benesi, J. Magn. Reson. **143**, 153 (2000).
[27] G. Otting, H. Widmer, G. Wagner, and K. Wüthrich, J. Magn. Reson. **187**, 187 (1986).
[28] B. Blümich, P. Blumler, and J. Jansen, Solid State NMR **1**, 111 (1992).
[29] D. Massiot, J. Hiet, N. Pellerin, F. Fayon, M. Deschamps, S. Steuernagel, and P. J. Grandinetti, J. Magn. Reson. **181**, 310 (2006).
[30] While the TOP shear factors given here are the same as those given by Davis et al.[16], the scaling factor given by Davis et al.[16] was incorrect.
[31] M. Eden and M. H. Levitt, J. Magn. Reson. **132**, 220 (1998).
[32] W. H. Press, S. A. Teukolsky, W. T. Vetterling, and B. P. Flannery, *Numerical Recipes* (Cambridge University Press, 40 West 20th Street, New York, NY 10011, 1992).
[33] M. Strohmeier, D. Alderman, and D. M. Grant, J. Magn. Reson. **155**, 263 (2002).
[34] K. Dey, J. T. Ash, N. M. Trease, and P. J. Grandinetti, J. Chem. Phys. **133**, 05401 (2010).
[35] H. Y. Carr and E. M. Purcell, Phys. Rev. **94**, 630 (1954).
[36] S. Meiboom and D. Gill, Rev.Sci.Instrum **29**, 688 (1958).
[37] P. Zhang, C. Dunlap, P. Florian, P. J. Grandinetti, I. Farnan, and J. F. Stebbins, J. Non. Cryst. Solids **204**, 294 (1996).
[38] P. Zhang, P. J. Grandinetti, and J. F. Stebbins, J. Phys. Chem. B **101**, 4004 (1997).
[39] M. Davis, D. C. Kaseman, S. M. Parvani, K. J. Sanders, P. J. Grandinetti, P. Florian, and D. Massiot, J. Phys. Chem. A **114**, 5503 (2010).
[40] M. Davis, K. J. Sanders, P. J. Grandinetti, S. J. Gaudio, and S. Sen, J. Non. Cryst. Solids **357**, 2787 (2011).
[41] W. T. Dixon, J. Magn. Reson. **64**, 332 (1985).
[42] M. H. Levitt, J. Magn. Reson. **82**, 427 (1989).
[43] W. T. Dixon, J. Magn. Reson. **44**, 220 (1981).

Appendix C

$Q^{(3)}$-site Variations in a Mixed Potassium/Magnesium Glass using Natural Abundance ^{29}Si Magic-Angle Flipping (MAF) NMR

Eric G. Keeler[a], Jay H. Baltisberger[b], Kevin J. Sanders[a], Derrick C. Kaseman[a], Philip J. Grandinetti[a,*]

[a]*Department of Chemistry, The Ohio State University, 120 W. 18th Avenue, Columbus, Ohio 43210-1173*
[b]*Division of Natural Science, Mathematics, and Nursing, Berea College, Berea, Kentucky 40403*

Abstract

In this paper present new data on mixed modified tetra-silicate glass of composition (1-z)[$K_{2x}Mg_{(1-x)}O \cdot 4SiO_2$] $\cdot$ zCuO where x = 1, 0.875, 0.75, 0.625, and 0.5, and z $\sim$ 0.004. This glass, with compositions of x = 1 and 0.5, was studied with ^{17}O dynamic-angle spinning (DAS) NMR in 1992 by Farnan and coworkers [1] and it was shown that there was considerable order of the non-bridging oxygen sites. We studied the ^{29}Si sites using two-dimensional magic-angle flipping (2D MAF) NMR at natural abundance to examine the degree to which this clustering can be observed in a range of glass compositions. A nuclear shielding anisotropy, ζ, of 84.3 $\pm$ 0.1 ppm for the x = 1 sample and 59.9 $\pm$ 0.2 ppm for the x = 0.5 sample were determined based on a two site simulation of the MAF spectra. The two sites for these various $Q^{(3)}$ sites are labelled as site 1 for the x = 1 sample and site 2 for the x = 0.5 sample. The nuclear shielding anisotropy of the x = 1 sample corresponds to a pure potassium coordination environment; whereas the nuclear shielding anisotropy of the x = 0.5 sample is corresponds to a mixed potassium/magnesium coordination environment, which is proposed as a $K_{2i} \cdot Mg_i$, where the potassium-to-magnesium ratio is believed to be restrictive but the total number of modifier cations near each non-bridging oxygen is no known. A three site simulation was used to fit the other glasscompositions and two distinct anisotropic lineshapes were found with: $\zeta_{site\ 1}$ = 86.3 $\pm$ 1.1 ppm and $\zeta_{site\ 2}$ = 63.9 $\pm$ 4.8 ppm for the x = 0.875 sample, $\zeta_{site\ 1}$ = 85.7 $\pm$ 0.4 ppm and $\zeta_{site\ 2}$ = 58.1 $\pm$ 0.3 ppm for the x = 0.75 sample, and $\zeta_{site\ 1}$ = 87.9 $\pm$ 0.6 ppm and $\zeta_{site\ 2}$ = 62.4 $\pm$ 0.3 ppm for the x = 0.625 sample corresponding to the same cation clustering coordination environments from the x = 1 and x = 0.5 samples. *Ab initio* quantum chemical calculations were performed on a basic silicate tetrahedron built to simulate various $Q^{(n)}$-species with different Si-NBO bond distances to investigate the experimentally determined trend between the network modifying cation potential and the nuclear shielding anisotropy. Both the experimental and theoretical *ab initio* calculations indicate that as cations with larger cation potential are incorporated into the glass then the magnitude of the nuclear shielding anisotropy increases.

Keywords: ^{29}Si NMR, natural abundance, Magic-Angle Flipping, nuclear shielding tensor, alkali and alkaline earth silicate glass, *ab initio*

1. Introduction

The bulk thermodynamic and transport properties of noncrystalline solids are determined by their atomic-level structure and therefore it is important to understand the structure of noncrystalline solids [2–4]. Understanding the structure and composition of noncrystalline solids can allow for materials to be made for a particular property due to the fact that their properties vary continuously with composition [5, 6]. However, theoretical models are

*To whom correspondence should be addressed. Email: grandinetti.org/Contact.

not yet able to accurately relate structure to properties, which makes the design of noncrystalline solids for particular properties difficult. Silicate glasses are known to be composed of silicate tetrahedra that are interlinked through bridging oxygen bonds. When network modifying cations are incorporated into the glass then this structure is broken and silicon non-bridging oxygen (NBO) bonds are formed. The network modifying cations coordinate near the NBO sites within the glass structure; however, the degree of order that is associated with each coordination near non-bridging oxygen sites within the glass is not well known.

Previous studies by Greaves et al. [7, 8] using X-ray absorption fine structure (EXAFS) determined that the network modifying cations are regularly coordinated to the NBO sites in silicate glasses. Neutron diffraction studies [9, 10] have shown that the ordering of network modifying cations extends beyond the local bonding environment into the intermediate bonding environment by the determination of strong correlations between Ca-Ca and Ca-O distances in $CaSiO_3$ glasses. Nuclear magnetic resonance (NMR) has been routinely used to study the order, or disorder, of network modifying cations within the structure of glasses with only a single network modifying cation [1, 11–17]. However, few studies [1, 11] have utilized NMR to understand how the glass structure changes when two or more different modifying cations are present.

The use of two-dimensional magic-angle flipping (2D MAF) NMR has been shown, in previous studies [12, 13], to give over an order of magnitude improvement in quantification of $Q^{(n)}$-species concentrations in comparison to conventional Magic-Angle Spinning (MAS) lineshape analysis. 2D MAF NMR produces a two dimensional spectrum correlating isotropic and anisotropic nuclear shielding contributions. 2D MAF NMR has been utilized by Davis et al. [14, 15] to understand how the magnitude of the nuclear shielding anisotropy changes for samples containing different modifying cations. A clear trend was observed indicating that as cations with higher cation potential, defined as the charge of the cation divided by the atomic

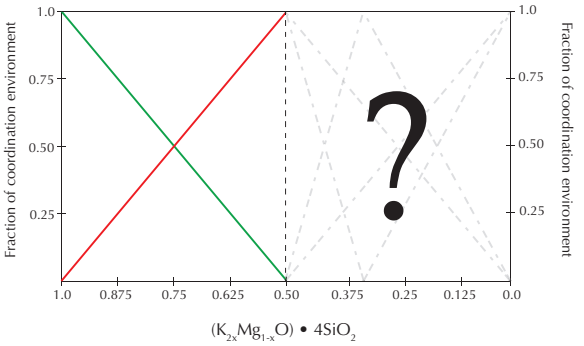

Figure 1: A binary model for the cation clustering coordination environments of the $K_{2x}Mg_{1-x}O \cdot 4SiO_2$ glass based on the previous ^{17}O DAS results [1]. The red line represents a pure potassium coordination environment; while, the green line represents a mixed potassium/magnesium coordination environment. The mixed coordination environment is proposed to be $K_{2i} \cdot Mg_i$. The coordination environments for the compositions $x < 0.5$ are unknown; however, several possible linear distributions of cation coordination environments are shown, gray dashed lines.

radius, were incorporated in the glass structure, the nuclear shielding anisotropy should linearly decrease. Using trends initially reported by Grimmer and coworkers [18, 19], this change in the nuclear shielding anisotropy was related to a changing Si-NBO bond length. It was proposed that as cations with higher cation potential are incorporated into the glass, the Si-NBO bond length must therefore be decreasing. These studies, however, focused on analyzing silicate glasses with a single modifying cation.

When multiple network modifying cations are introduced into the glass structure the cation coordination environment near each non-bridging oxygen site is not only dependent on the total number of cations coordinated to the oxygen but also which particular cations are present near the NBO site. Therefore, the number of cation coordination environments within the glass structure is greatly increased with the addition of multiple network modifying cations. This increase in the possible number of cation coordination environment indicates that there could be multiple anisotropic nuclear shielding interactions for a particular $Q^{(n)}$ site within the glass structure.

In this paper we present new results on a previously studied mixed potassium/magnesium tetrasilicate glass [1], of composition $K_{2x}Mg_{1-x}O \cdot 4SiO_2$, where Farnan and coworkers determined, via ^{17}O dynamic angle spinning (DAS) NMR, that there was one unique cation clustering coordination environment for the $K_2O \cdot 4SiO_2$ glass and one unique cation clustering environment for the $K_{1.0}Mg_{0.5}O \cdot 4SiO_2$ glass. These were the only two compositions that were previously studied. Therefore, the cation clustering environment in the $K_2O \cdot 4SiO_2$ (x = 1) glass must be a pure potassium environment, while the cation clustering environment in the $K_{1.0}Mg_{0.5}O \cdot 4SiO_2$ (x = 0.5) glass must be a mixed potassium/magnesium coordination environment. This suggests a surprising amount of ordering of the network modifying cations within this mixed modified silicate glass.

In Figure 1, we present a model for cation clustering coordination distributions in all compositions of the glass, based on these previous results. This model assumes a binary distribution of the two unique cation clustering coordination environments; therefore, at any given composition between the x = 1 and the x = 0.5 compositions both cation coordination environments must be present at varying concentrations. The green line represents a pure potassium coordination environment around the non-bridging oxygen, while the red line represents a mixed potassium/magnesium coordination environment. The mixed potassium/magnesium coordination environment that is proposed is a $K_{2i} \cdot Mg_i$ coordination, where we believe that the potassium-to-magnesium ratio is somewhat restrictive. However, the exact number of cations clustering to each non-bridging oxygen is not known. Any number of different coordination environments could be present with linear or non-linear dependencies on composition for compositions of x < 0.5. Therefore, only a few possible coordination environments are proposed (all linearly dependent on composition), the gray dashed lines, including distributions of pure magnesium coordination, the $K_{2i} \cdot Mg_i$ coordination environment, and a different mixed potassium and magnesium environment, $K_i \cdot Mg_i$. However, there is no evidence to suggest any particular distribution of any of these coordination environments is present in these richer magnesium compositions of the glass.

2. Experimental

2.1. Sample Preparation

Five samples were prepared with the compositions (1-z)$[K_{2x}\ Mg_{(1-x)}O \cdot 4SiO_2] \cdot zCuO$, where x = 1, 0.875, 0.75, 0.625, and 0.5 and z ~ 0.004. Approximately 2g of each sample was synthesized from K_2CO_3 (Aldrich, 99+%), MgO (Alfa Aesar, 99.95%), SiO_2 (Aldrich, 99.995%), and CuO (Mallinckrodt). Prior to synthesis the K_2CO_3 and MgO were placed in a dehydrating furnace at 150°C overnight to remove any water from the sample. The starting materials were ground and placed in a furnace at 600°C overnight to decarbonate followed by melting at 1100°C for the x = 1 and 0.875 compositions, 1300°C for the x = 0.75 and 0.625 compositions, and 1400°C for the x = 0.5 composition for 1.5 hours. Each sample was quenched by placing the bottom of the platinum crucible in water. Each sample was ground into a powder and packed in a rotor in a nitrogen filled glove bag. We found that doping with Cu(II), which has a short $T_{1,e}$, reduced the ^{29}Si T_1 without significantly reducing the ^{29}Si T_2. While the relaxation times for some of our undoped samples exceeded 1000s, doping with approximately 0.004 mole fraction CuO reduced the relaxation delay by a factor of 20. An elemental analysis, results shown in Table 1, was performed by Galbraith Laboratories (Knoxville, Tennessee) to determine the exact composition of each glass sample. The proper stoichiometric compositions of each glass are shown in Table 1 and will be used in all following tables and figures.

2.2. Nuclear Magnetic Resonance

All experiments were performed on a Tecmag Apollo NMR spectrometer operating at a field strength of 9.4 Tesla (79.474 MHz for ^{29}Si) using

Table 1: Elemental analysis showing the relative population, in weight percent, of each element in each composition and the proper composition of each sample.

Glass sample	Silicon	Potassium	Magnesium	Proper Composition
x = 1	33.6%	22.7%	–	$0.996(K_2O \cdot 4SiO_2) \cdot 0.004CuO$
x = 0.875	34.3%	20.9%	0.9%	$0.996(K_{1.75}Mg_{0.125}O \cdot 4SiO_2) \cdot 0.004CuO$
x = 0.75	35.0%	18.3%	1.9%	$0.996(K_{1.5}Mg_{0.25}O \cdot 4SiO_2) \cdot 0.004CuO$
x = 0.625	35.7%	15.5%	2.9%	$0.996(K_{1.25}Mg_{0.375}O \cdot 4SiO_2) \cdot 0.004CuO$
x = 0.5	36.5%	12.7%	4.0%	$0.996(K_{1.0}Mg_{0.5}O \cdot 4SiO_2) \cdot 0.004CuO$

homebuilt 4mm (for the x = 1, 0.75, and 0.5 compositions) 7mm (for the x = 0.875, 0.625 compositions) DAS probes each based on a previous design [20]. Spin lattice relaxation times, T_1, were determined by the saturation recovery experiment. The relaxation curves were found to be multi-exponential and were best fit with a stretched exponential function. The time for 75% of the signal maximum to have recovered for each composition and the recycle delays that were used for each experiment are shown in Table 2.2.

The recycle delay was initially set (for the x = 0.5 and 0.75 compositions) such that full relaxation ($5T_1$) was achieved throughout the sample. However, to further enhance the signal-to-noise ratio (S/N) of the experiments, the recycle delay for the x = 0.75 composition ($K_{1.5}Mg_{0.25}O \cdot 4SiO_2$) was set to 10 seconds, which was less than $\frac{1}{4}T_1$, to allow for a large number of scans to be performed in an identical amount of time. The two 2D MAF spectra were processed identically and a S/N enhancement of 2 times was achieved. The spectra were properly scaled by their signal maxima, and then subtracted from one another to yield residuals that were purely noise. This gave evidence that the copper dopant was evenly distributed throughout the glass structure and that all silicon centers were being relaxed equally. Therefore, the recycle delay was truncated to shorter than full relaxation for the remaining compositions to allow for greater sensitivity and shorter experiment times.

The 2D MAF experiment correlates MAS frequencies to anisotropic frequencies obtained while spinning off the magic angle during the τ_{echo} evolution period. The detection angle, θ_R, used in this

Table 2: Relaxation times and recycle delays for each composition.

Glass composition	75% time / s	Recycle delay / s
$K_2O \cdot 4SiO_2$	17.3	60.0
$K_{1.75}Mg_{0.125}O \cdot 4SiO_2$	11.3	20.0
$K_{1.5}Mg_{0.25}O \cdot 4SiO_2$	43.0	10.0 / 200
$K_{1.25}Mg_{0.375}O \cdot 4SiO_2$	20.0	7.0
$K_{1.0}Mg_{0.5}O \cdot 4SiO_2$	50.9	210

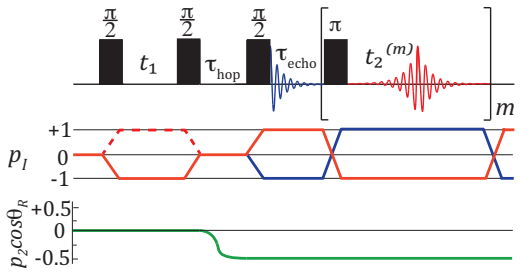

Figure 2: The shifted-echo Magic-Angle Flipping pulse sequence with CPMG echo train acquisition pulse sequence used for all experiments. The initial half-echo was acquired for only the x = 0.875 sample to enhance the signal-to-noise ratio of the experiment. Hypercomplex acquisition is performed to obtain positive and negative t_1 quadrants in the 2D time domain signal [21], as indicated by the dashed line.

experiment is 90°, or perpendicular to the external magnetic field direction, where the averaged anisotropic frequencies are scaled by a factor of $-\frac{1}{2}$ [22]. The original incarnation of the 2D MAF-CPMG experiment [15] detected at the magic angle due to the fact that the samples were 100% ^{29}Si-enriched and the homonuclear ^{29}Si-^{29}Si dipolar interactions lead to a rapid dephasing of the signal and echo train when detection is performed away from the magic angle. However, in the natural abundance samples that were studied for this paper detection at 90% from the external magnetic field causes the echo time to be shorter; therefore, more echoes can be detected in the same period of time. The 2D MAF spectra were obtained using the shifted-echo MAF pulse sequence [23, 24] with CPMG [25, 26] echo-train acquisition, as shown in Figure 2, to enhance sensitivity due to the low isotopic abundance (~4.7%) and NMR frequency of ^{29}Si. The initial half-echo was acquired, for the x = 0.875 composition, processed separately and added to the rest of the processed data to further enhance the signal-to-noise ratio. An exponential line apodization of approximately 3 Hz was applied to the echo dimension of each spectrum to enhance the sensitivity. All 2D MAF figures are displayed with the 90° dimension being nuclear shielding; therefore, the 90° dimension appears as increasing from left to right. In the discussion that follows we employ the IUPAC definition for the nuclear shielding and chemical shift interactions [27]. The isotropic nuclear shielding is defined as the trace of the nuclear shielding tensor,

$$\sigma_{iso} = \frac{1}{3}(\sigma_{zz} + \sigma_{yy} + \sigma_{xx}) \quad (1)$$

where, σ_{zz}, σ_{yy}, and σ_{xx} are the principal components of the second-rank shielding tensor. The nuclear shielding tensor can be thought of as an ellipsoid in three-dimensional space; however, this is best understood if the isotropic nuclear shielding is subtracted from the diagonal components of the nuclear shielding tensor,

$$\lambda_{zz} = \sigma_{zz} - \sigma_{iso}, \quad (2)$$

$$\lambda_{yy} = \sigma_{yy} - \sigma_{iso}, \quad (3)$$

$$\lambda_{xx} = \sigma_{xx} - \sigma_{iso}. \quad (4)$$

In this reference frame the λ values describe deviations, positive or negative, from a perfect sphere. The isotropic chemical shift is defined as

$$\delta_{iso} = \frac{\sigma_{ref} - \sigma_{iso}}{1 - \sigma_{ref}} \quad (5)$$

where, σ_{ref} is the nuclear shielding of the reference compound, TMS for this study. The nuclear shielding anisotropy is defined as

$$\zeta = \sigma_{zz} - \sigma_{iso} \quad (6)$$

when the Haeberlen convention [27], where

$$|\sigma_{zz} - \sigma_{iso}| > |\sigma_{yy} - \sigma_{iso}| > |\sigma_{xx} - \sigma_{iso}|, \quad (7)$$

is adopted. The notation, $\zeta_{site\ m}$, will be used for the different nuclear shielding anisotropy values for the same $Q^{(n)}$ sites, where m indicates the arbitrary number assigned for that nuclear shielding anisotropy value.

2.3. Ab Initio Calculations

The nuclear shielding tensors were investigated using *Gaussian 03* [28] at a Hartree-Fock level with a 6-311+G(2d,p) basis set used for all atoms using the gauge-independent atomic orbitals (GIAO) mehtod. Calculations were performed on silicon centered clusters, as shown in Figure 3, that were built in the axis system shown to the right of each cluster (the axis not shown in both A and B of Figure 3 is positive coming out of the page). The clusters were built to simulate different silicate tetrahedra with varying Si-NBO bond distance to emulate the bonding environment in $Q^{(n)}$-species with various modifier cations. These clusters were built in their principal axis system with respect to the perturbation of the Si-O bond distances that was to be performed. A $Q^{(4)}$ environment, using a Si-O bond distance of 1.61 Å based on the bond distance of α-quartz [19, 29] was used as the starting point for the clusters, with hydrogens bonded to the end of each oxygen anion and held at a bond angle of 180° to balance the charge of the cluster (not shown).

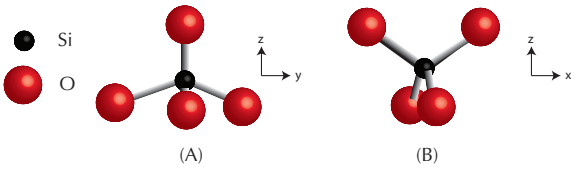

Figure 3: The silicon centered clusters were built in their principal axis system, shown to the right of each cluster, with respect to the perturbation dependent on the $Q^{(n)}$-species that was being simulated. (A) the $Q^{(3)}$ and $Q^{(1)}$ cluster is shown, and (B) the $Q^{(2)}$ cluster is shown.

The $Q^{(3)}$ clustering environment was made from the cluster shown in Figure 3A by decreasing the Si-O bond at the top of the cluster, by 0.01 Å from 1.61 Å to 1.51 Å . This depression of the Si-O bond distance simulates the changing Si-NBO bond distance in the presence of different network modifying cations. The $Q^{(2)}$-like cluster was made by decreasing the Si-O bond distance of two the bonds at the top of the cluster shown in Figure 3B to 1.51 Å in steps of 0.01 Å. The $Q^{(2)}$ clusters were simulated by a symmetric depression of the two Si-NBO bonds, which is meant to simulate a $Q^{(2)}$ site with a single modifying cation. The $Q^{(1)}$ cluster was built using the same starting cluster as the $Q^{(3)}$ cluster; however, the Si-O bond was stretched to 1.71 Å, by 0.01 Å, to simulate the perturbed oxygen as the bridging oxygen and the other three oxygens as non-bridging oxygens. This difference in the bond that is being changed has no effect on how the tensor changes based on the change in bonding environment near the ^{29}Si nucleus. The changing Si-O bond distance should in theory be placing more (shorter bond distance) or less (longer bond distance) electron density near the ^{29}Si nucleus.

3. Results and Discussion

3.1. 2D MAF NMR

The MAS spectrum of each composition contains a broad resonance with two distinct peaks centered around δ_{iso} = -105 ppm and δ_{iso} = -95 ppm. The presence of these two unique isotropic chemical shifts is consistent with overlapping $Q^{(4)}$ (δ_{iso} = -105 ppm) and $Q^{(3)}$ (δ_{iso} = -95 ppm) resonances. Figures 4–8 show the 2D contour plots of the MAF spectra for all compositions, where the two distinct isotropic chemical shifts can be clearly seen in the 1D projection along the isotropic dimension (vertical axis). Note that there is a clear diagonal line of noise present in all of the MAF spectra (at 3 kHz before the shear is applied), which is due to the stepper motor that is being used for angle hopping. This characteristic noise can be ignored due to the fact that it does intersect any of the data and therefore does not affect the fitting of the 2D spectra.

Each $Q^{(n)}$-species has well-defined differences in the ^{29}Si nuclear shielding tensor, which manifest as a distinct anisotropic lineshape [12, 13]. In Figures 4–8, the MAS lineshape is clearly dominated by $Q^{(4)}$ near δ_{iso} = -105 ppm and by $Q^{(3)}$ near δ_{iso} = -95 ppm based on their distinct anisotropic lineshapes found in the 90° dimension (horizontal axis). Each 2D spectrum was simulated using a Gaussian distribution of isotropic shifts for each site in the glass sample. The anisotropic lineshape for each $Q^{(n)}$ site was modeled by four parameters: (1) a Gaussian line broadening, (2) the isotropic chemical shift, δ_{iso}, (3) the nuclear shielding anisotropy, ζ, and (4) the integrated intensity of each $Q^{(n)}$ site. No constraints were placed on any of the four parameters that were being used to model the anisotropic lineshape for each $Q^{(n)}$ site. Therefore, all of the parameters varied freely throughout the simulations.

The best fit values for the nuclear shielding anisotropy for each $Q^{(n)}$ site and the relative fraction for each $Q^{(n)}$ site are shown in Table 3. While, the mean and width of the isotropic chemical shift distributions for each $Q^{(n)}$ site are shown in Table 4. Previous work by Farnan et al. [1] suggested that the x = 1 and 0.5 compositions had a single unique nuclear shielding anisotropy; therefore, the x = 1 and 0.5 spectra were simulated assuming a two site model, one $Q^{(3)}$ and one $Q^{(4)}$ site. The nuclear shielding anisotropy for the $Q^{(4)}$ was assumed to be nearly zero and was held constant across all isotropic shift values. The nuclear

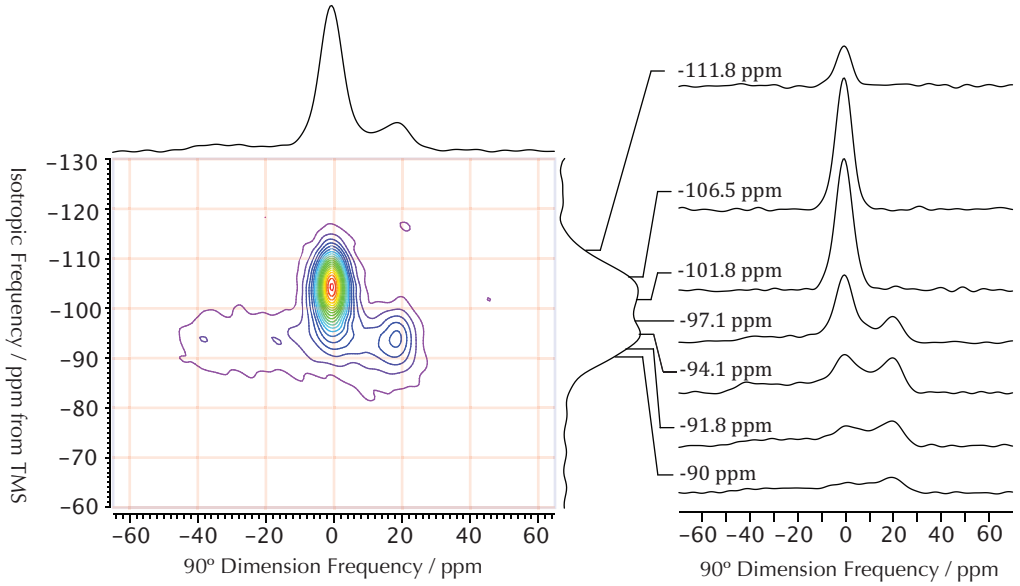

Figure 4: 2D MAF-CPMG spectrum of $K_2O \cdot 4SiO_2$ glass. One dimensional projections are provided onto the MAS and 90° dimensions. Selected cross sections of the 90° dimension are presented to the right of the 2D spectrum. The 90° dimension is nuclear shielding and not chemical shift.

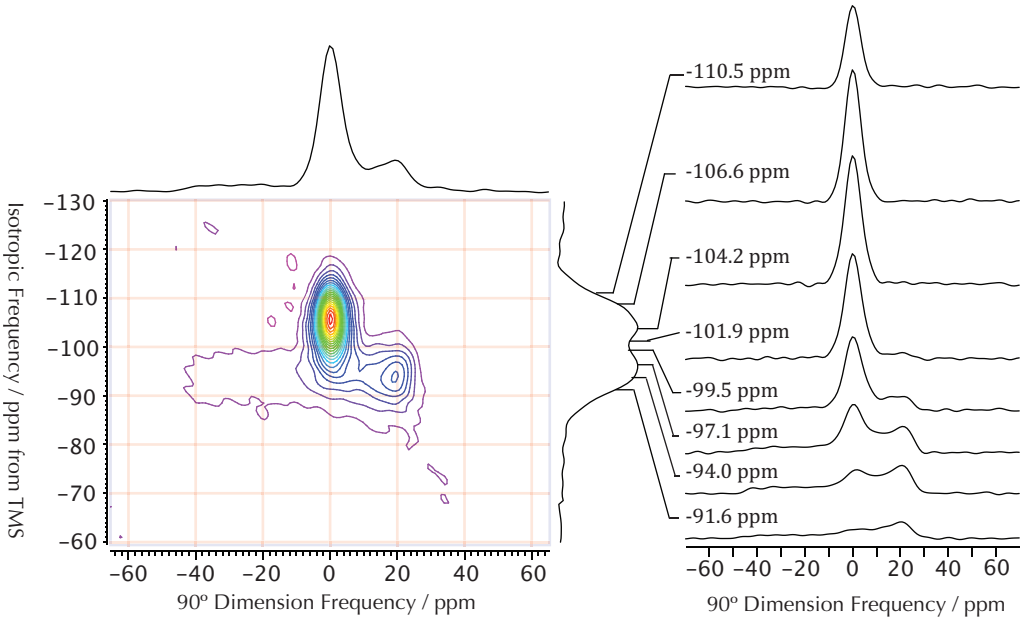

Figure 5: 2D MAF-CPMG spectrum of $K_{1.75}Mg_{0.125}O \cdot 4SiO_2$ glass. One dimensional projections are provided onto the MAS and 90° dimensions. Selected cross sections of the 90° dimension are presented to the right of the 2D spectrum. The 90° dimension is nuclear shielding and not chemical shift.

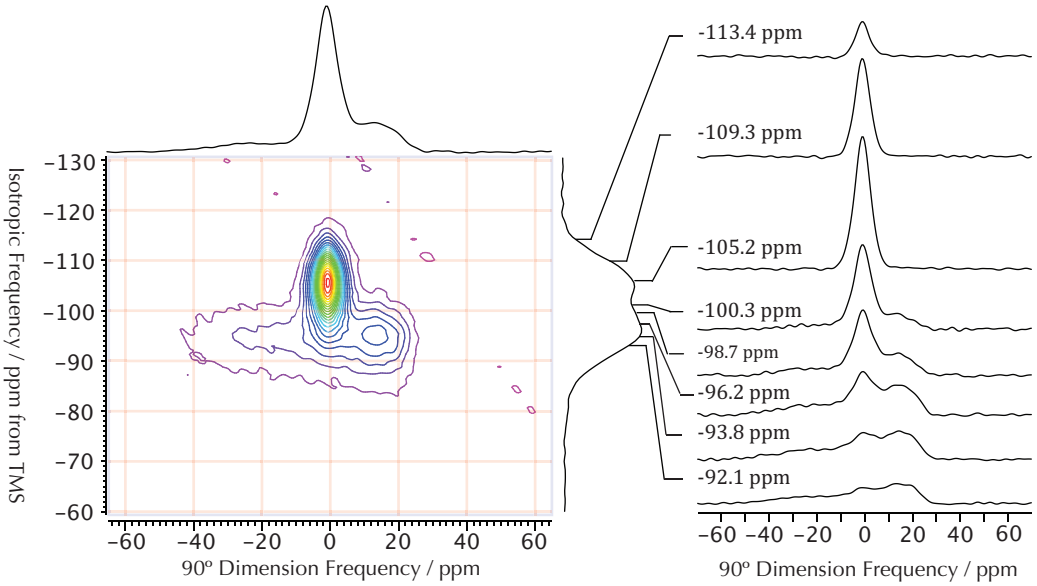

Figure 6: 2D MAF-CPMG spectrum of $K_{1.5}Mg_{0.25}O \cdot 4SiO_2$ glass when a recycle delay of 10 seconds was used. The residuals of the experiment where the recycle delay was set to 200 seconds and the experiment shown were found to be noise. One dimensional projections are provided onto the MAS and 90° dimensions. Selected cross sections of the 90° dimension are presented to the right of the 2D spectrum. The 90° dimension is nuclear shielding and not chemical shift.

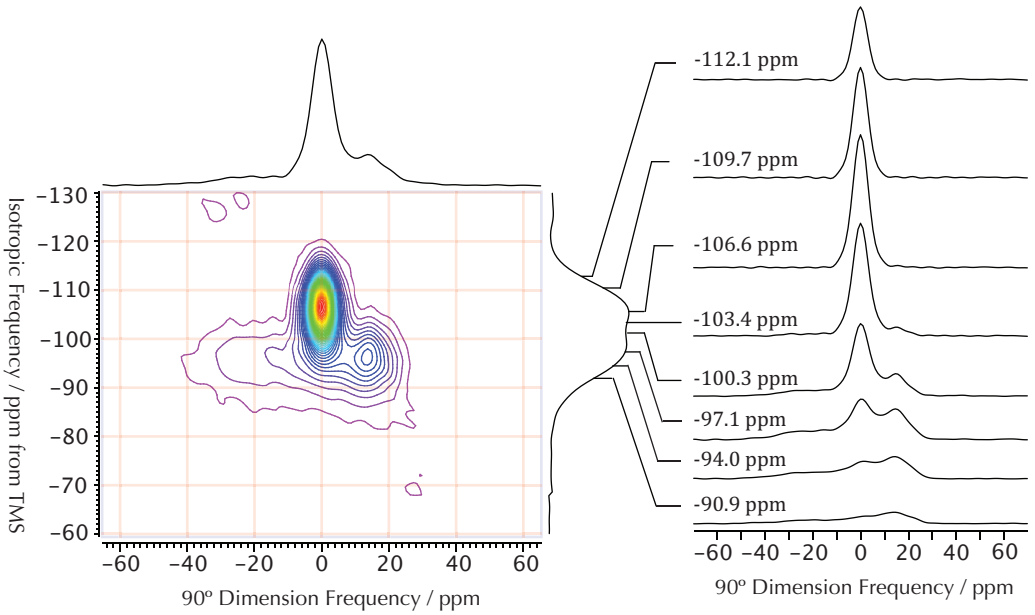

Figure 7: 2D MAF-CPMG spectrum of $K_{1.25}Mg_{0.375}O \cdot 4SiO_2$ glass. One dimensional projections are provided onto the MAS and 90° dimensions. Selected cross sections of the 90° dimension are presented to the right of the 2D spectrum. The 90° dimension is nuclear shielding and not chemical shift.

shielding anisotropy of the $Q^{(3)}$ site was also held constant across the isotropic chemical shift distribution; however, the anisotropy, ζ, in the x = 1 composition was determined to be 84.3 ± 0.1 ppm, while for the x = 0.5 it was found to be 59.9 ± 0.2 ppm, as shown in Table 3. The nuclear shielding anisotropy for the $Q^{(3)}$ site associated with a pure potassium clustering environment is labelled as $\zeta_{site\ 1}$; whereas, the mixed potassium/magnesium clustering environment is labelled as $\zeta_{site\ 2}$.

Therefore, a distinct nuclear shielding anisotropy, ζ, for the x = 1 and 0.5 compositions was found, in agreement with the previous ^{17}O results [1]. The x = 0.5 sample, which has a composition of $K_{1.0}Mg_{0.5}O \cdot 4SiO_2$, has equal, by charge, populations of potassium and magnesium. Therefore, the cation clustering coordination in the x = 0.5 composition is believed to be the $K_{2i} \cdot Mg_i$ coordination environment that was proposed earlier. This mixed cation clustering environment has a potassium-to-magnesium ratio that is thought to be somewhat restrictive; however, the exact number of modifying cations is not known. The nuclear shielding anisotropy, ζ, for the x = 1 ($K_2O \cdot 4SiO_2$) and 0.5 ($K_{1.0}Mg_{0.5}O \cdot 4SiO_2$) compositions were determined to be in agreement with previously reported trends [14, 16] for varying network modifying cation potential. The nuclear shielding anisotropy for the $K_{2i} \cdot Mg_i$ coordination environment was determined to be between previous results for pure potassium and pure magnesium silicate glasses. Therefore, the Si-NBO bond distance for the $K_{2i} \cdot Mg_i$ coordination environment is believed to be between the Si-NBO bond distance for pure potassium and pure magnesium silicate glasses.

According to the earlier proposed binary model the x = 0.875 ($K_{1.75}Mg_{0.125}O \cdot 4SiO_2$), x = 0.75 ($K_{1.5}Mg_{0.25}O \cdot 4SiO_2$), and x = 0.625 ($K_{1.25}Mg_{0.375}O \cdot 4SiO_2$) compositions are believed to have two distinct $Q^{(3)}$ sites with a differing relative population in each distinct $Q^{(3)}$ site. These compositions were simulated with the same two site (one $Q^{(4)}$ site and one $Q^{(3)}$ site) as the x = 1 and 0.5 compositions, as shown for the x = 0.75 composition in Figure 9A; however, when a three site model was employed, Figure 9B, the simulation was determined to be a better fit for the experimental data than the two site model. Therefore, by assuming a three site model for the x = 0.875, 0.75, and 0.625 compositions and using the nuclear shielding anisotropy parameters from the x = 1 and 0.5 compositions as a starting point, each spectrum was fit with good reduced chi-squared values, shown in Table 3.

The nuclear shielding anisotropy for each site in the compositions was found to be similar to the original starting parameters; however, due to factors that were not accounted for, such as non-identical experimental conditions, or slight disparities in composition, the ζ for each site in each composition were not found to be identical. However, it is believed that the nuclear shielding anisotropy for the distinct $Q^{(3)}$ sites in each composition correspond to the same cation clustering coordination environment. The large error that is present on $\zeta^{(3)}_{site\ 2}$ for the x = 0.875 composition is likely due to the low fraction of that $Q^{(3)}$ within the composition and the fact that the narrower $Q^{(3)}_{site\ 2}$ lineshape is difficult to fit underneath the wider and more abundant $Q^{(3)}_{site\ 1}$ lineshape. Therefore, the fitting of the three site model was most difficult to implement on the x = 0.875 composition because the low fraction of the wider $Q^{(3)}_{site\ 1}$ lineshape in the x = 0.625 sample can be fit with relative ease, as evidenced by the large errors in Table 3. The relative ease with which the x = 0.625 sample can be fit is due to the least abundant $Q^{(3)}$ lineshape is the wider site 1 lineshape and therefore it is not hidden underneath a wider more abundant lineshape like the fit for the x = 0.875 sample.

The relative populations of the two $Q^{(3)}$ sites were calculated based on the integrated intensity of each $Q^{(n)}$ from the fit and are shown in Table 3. The errors for all parameters were calculated using the bootstrap resampling method during the simulations [30] and are reported as one standard deviation ($\pm 1\sigma$). The relative populations of the two distinct $Q^{(3)}$ sites in each composition were determined to be in good agreement with the bi-

Table 3: The reduced-chi-squared value, χ^2_ν, the nuclear shielding anisotropy, ζ for both sites, the relative fraction for the $Q^{(4)}$ and $Q^{(3)}$ sites in each glass, and the relative fraction of both $Q^{(3)}$-species within each glass composition. The errors reported are $\pm 1\sigma$ and were determined by bootstrap resampling [30] during the simualtions.

Glass composition	χ^2_ν	$\zeta_{site\ 1}$ / ppm	$\zeta_{site\ 2}$ / ppm	Relative $Q^{(3)}$ fraction	Relative $Q^{(4)}$ fraction	Relative fraction of $Q^{(3)}$ for site 1	Relative fraction of $Q^{(3)}$ for site 2
$K_2O \cdot 4SiO_2$	1.58 ± 0.02	84.3 ± 0.1	–	0.464 ± 0.003	0.536 ± 0.002	1	–
$K_{1.75}Mg_{0.125}O \cdot 4SiO_2$	1.35 ± 0.03	86.3 ± 1.1	63.9 ± 4.8	0.49 ± 0.04	0.51 ± 0.04	0.79 ± 0.06	0.21 ± 0.06
$K_{1.5}Mg_{0.25}O \cdot 4SiO_2$	1.68 ± 0.02	85.7 ± 0.4	58.1 ± 0.3	0.508 ± 0.005	0.492 ± 0.005	0.512 ± 0.005	0.488 ± 0.004
$K_{1.25}Mg_{0.375}O \cdot 4SiO_2$	2.19 ± 0.17	87.9 ± 0.6	62.4 ± 0.3	0.47 ± 0.01	0.53 ± 0.01	0.250 ± 0.007	0.75 ± 0.02
$K_{1.0}Mg_{0.5}O \cdot 4SiO_2$	1.44 ± 0.02	–	59.9 ± 0.2	0.458 ± 0.003	0.542 ± 0.004	–	1

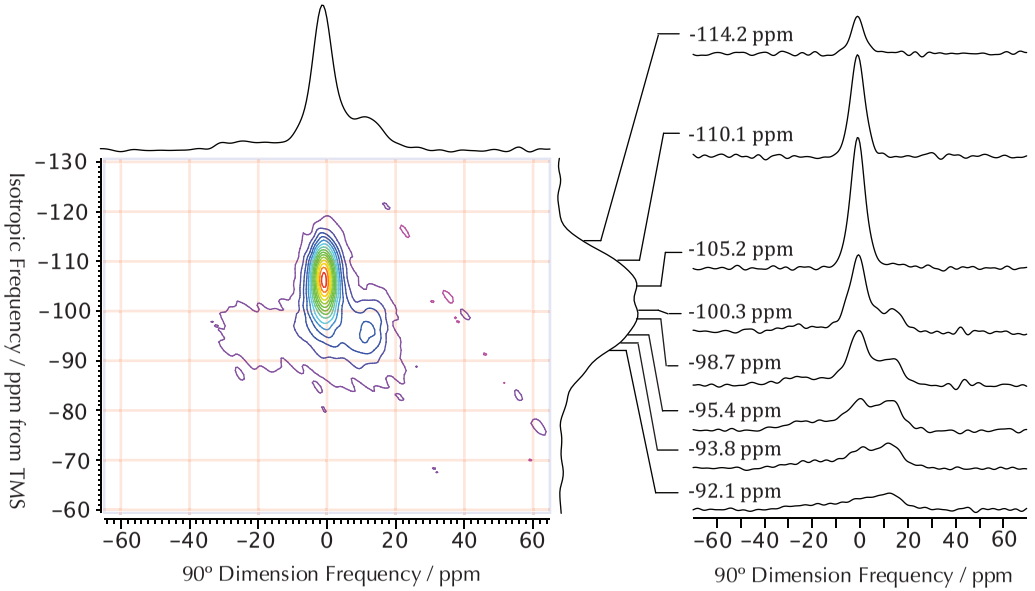

Figure 8: 2D MAF-CPMG spectrum of $K_{1.0}Mg_{0.5}O \cdot 4SiO_2$ glass. One dimensional projections are provided onto the MAS and 90° dimensions. Selected cross sections of the 90° dimension are presented to the right of the 2D spectrum. The 90° dimension is nuclear shielding and not chemical shift.

Table 4: The mean and width reported with $\pm 1\sigma$ errors determined from bootstrap resampling simulations [30] for the isotropic shift distributions of the $Q^{(n)}$ sites within each glass structure.

Glass composition	$\langle \delta^{(4)}_{iso} \rangle$ / ppm	Width / ppm	$\langle \delta^{(3)}_{iso,\ site\ 1} \rangle$ / ppm	Width / ppm	$\langle \delta^{(3)}_{iso,\ site\ 2} \rangle$ / ppm	Width / ppm
x = 1	-103.89 ± 0.08	7.13 ± 0.01	-93.29 ± 0.04	5.85 ± 0.02	–	–
x = 0.875	-105.4 ± 0.1	5.36 ± 0.04	-93.4 ± 0.2	4.8 ± 0.7	-96.0 ± 1.0	3.3 ± 0.2
x = 0.75	-105.50 ±0.09	5.10 ± 0.01	-94.1 ± 0.2	4.60 ± 0.04	-95.3 ± 0.3	4.63 ± 0.04
x = 0.625	-106.48 ± 0.06	5.37 ± 0.01	-93.1 ± 0.6	6.5 ± 0.2	-96.4 ± 0.2	4.75 ± 0.06
x = 0.5	-106.3 ± 0.2	5.32 ± 0.02	–	–	-95.7 ± 0.3	5.24 ± 0.04

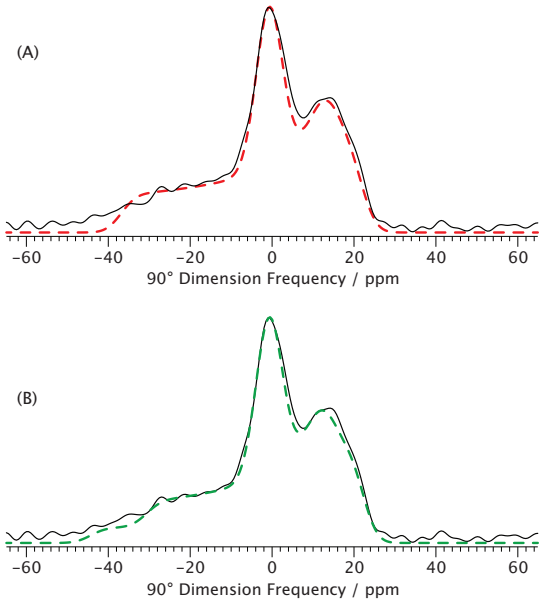

Figure 9: 1D cross section of the 2D MAF-CPMG spectrum of $K_{1.5}Mg_{0.25}O \cdot 4SiO_2$ glass at δ_{iso} = -97 ppm with respect to TMS. The experimental (solid line) cross section is shown with simulated cross sections (dashed lines) when a two site model (one $Q^{(4)}$ and one $Q^{(3)}$ site) was used (above, red line) and when a three site model (one $Q^{(4)}$ and two $Q^{(3)}$ sites) was used (below, green line). The dimension is displayed as nuclear shielding; therefore it is shown as increasing from left to right.

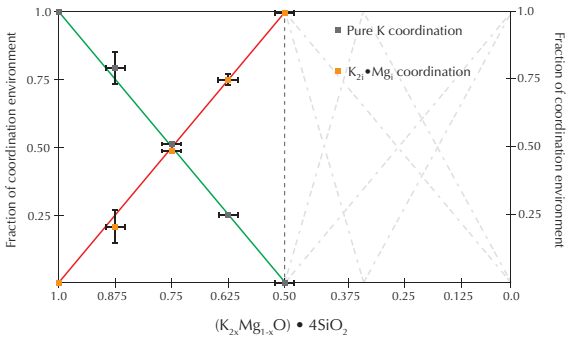

Figure 10: The binary model for the cation clustering coordination environments with the MAF results for each composition. The error bars reported for the fraction of each cation clustering environament (vertical dimension) are $\pm 1\sigma$ and are taken from Table 3. The points with no error bars have errors that are smaller than the size of the point and therefore the error bars are not visable. The error bars reported for the composition (horizontal axis) are from the elemental analysis of the glass samples.

nary model for the cation clustering environments around each non-bridging oxygen, as shown in Figure 10. Therefore, the network modifying cations coordinated near the NBO sites in this mixed magnesium/potassium tetra-silicate glass for all compositions, $1 \leq x \leq 0.5$, are believed to be found as a binary mixture of a pure potassium coordination environment and a $K_{2i} \cdot Mg_i$ mixed coordination environment. This suggests, in agreement with previous result, a considerable amount of ordering in the cation clustering within the glass structure.

In Figure 11, the ab initio calculations and the 2D MAF experimental results are combined

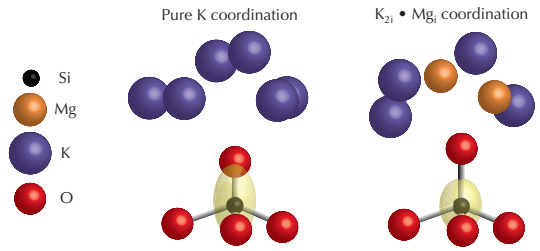

Figure 11: A model is presented for the cation clustering in the glass. The nuclear shielding tensors are represented based on the relative Si-NBO bond distance that is expected for each clustering environment determined from their nuclear shielding anisotropy from Table 3. A coordination of six modifier cations was chosen to represent the clustering environment; however, there are probably various numbers of cations modifying each non-bridging oxygen.

to create a model for the cation clustering environments within this mixed potassium/magnesium glass composition. The nuclear shielding tensors are shown based on the relative Si-NBO bond distance that is determined based on the nuclear shielding anisotropy determined from the MAF results. The number of modifier cations was chosen to be six based on an analysis of the oxygen anions using Pauling's rules [31]; however, there could be various numbers of modifier cations near each non-bridging oxygen.

3.2. Ab Initio Calculations

The nuclear shielding tensor parameters for the $Q^{(3)}$-like cluster, shown on the left side of Figure 12, were determined to become more shielded along the z-axis, while becoming deshielded along the x- and y-axes as the Si-NBO bond distance was decreased from the $Q^{(4)}$ α-quartz parameters. The λ_{zz} value shown is also the nuclear shielding anisotropy, ζ, for the cluster. Therefore, the nuclear shielding anisotropy, ζ, for the $Q^{(3)}$ cluster was determined to become greater as the Si-NBO bond distance decreased in agreement with the previously reported trend by Grimmer and coworkers [18, 19]. Thus, as the Si-NBO bond distance increases the electron density near the silicon nucleus decreases causing the z-axis to be deshielded. This is found to be in agreement with the correlation found by Davis et al. [14, 15] that as cations with higher cation potential are incorporated into the glass structure the Si-NBO bond distance increases causing the nuclear shielding anisotropy to decrease. This decrease in ζ corresponds to the nuclear shielding tensor becoming more symmetric due to the Si-NBO bond distance approaching the distance of the Si-BO bond distance. The cluster that is shown in the center of Figure 12, and on the right of Figure 13, represents the perfectly symmetric $Q^{(4)}$ environment and is shown with a perfectly spherical nuclear shielding tensor, represented by all zero λ values on the graph. The cluster that is shown in the top left corner of Figure 12 represents a $Q^{(3)}$ cluster that is modified by a weak cation, due to the short Si-NBO bond (1.51 Å). Based on the trends in the principal components of the nuclear shielding tensors the shape of the nuclear shielding tensor changes from a football along the z-axis to a perfect sphere as the cation potential of the network modifying cation are increased.

The $Q^{(1)}$ cluster calculations show, on the right of Figure 12 that the ^{29}Si nucleus becomes deshielded along the z-axis, while along the x- and y-axes the ^{29}Si nucleus becomes more shielded as the Si-NBO bonds were effectively decreased. The magnitude of the nuclear anisotropy, shown as λ_{zz} in Figure 12, of the $Q^{(1)}$ cluster was shown to be increasing with a decreasing Si-NBO bond distance, in agreement with the previous results reported by Grimmer [18, 19]. Due to the fact that the far right of the graph represents the shortest Si-NBO bonds, the cluster in the top right corner of Figure 12 is a representation of what the bonding environment of a silicate tetrahedron might be like in the presence of a weak network modifying cation. For this type of cluster the nuclear shielding tensor has effectively been perturbed from a perfect sphere into a pancake-like shape in the xy-plane. Therefore, as the cation potential of the network modifying cation in a $Q^{(2)}$ site is increased the nuclear tensor transforms from this shape into a sphere.

The $Q^{(2)}$ site cluster with a single network modifying cation was determined to become more deshielded along the y- axis, which is orthogo-

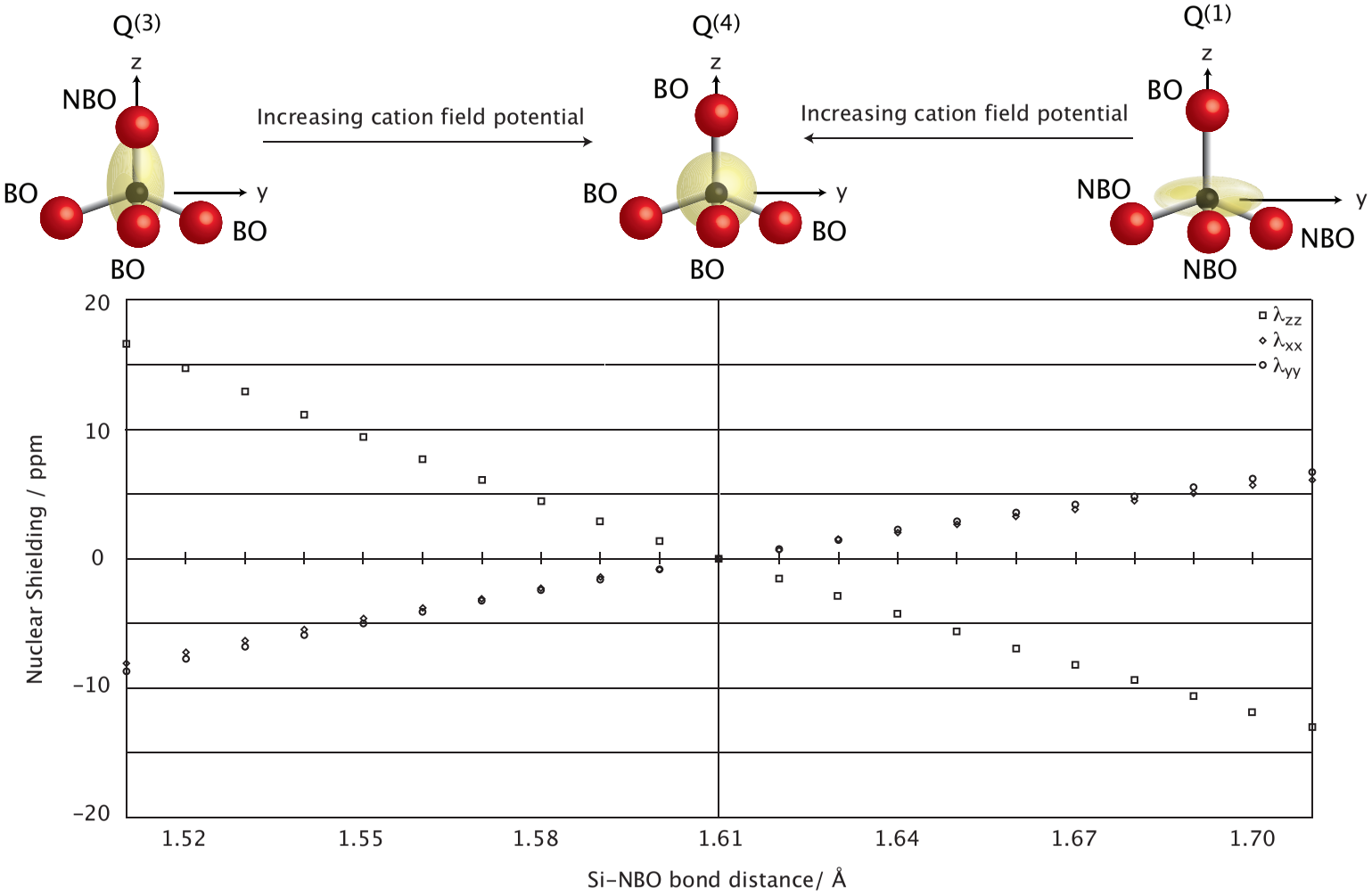

Figure 12: The *ab initio* computational results for the $Q^{(3)}$ (left side) and $Q^{(1}$ (right side) clusters for various Si-NBO bond distances. The Haeberlen convention has not been followed for the λ values shown and therefore the λ values correspond to their axis in the original (built) axis system. The nuclear shielding anisotropy for this axis system is defined as, λ_{zz} and therefore is shown to be in agreement with the previous results [14, 15, 18, 19]. The symmetric $Q^{(4)}$ cluster is shown in the middle above the graph with a spherical nuclear shielding tensor surrounding the ^{29}Si nucleus. The $Q^{(3)}$ cluster with a modifying cation (with a Si-NBO distance of 1.51 Å) is shown (top left) with a football-like tensor surrounding the ^{29}Si center. The cluster shown at the top right of the graph represents a $Q^{(1)}$ site with a Si-NBO bond distance of 1.51 Å for the and is shown with a pancake-like tensor surrounding the silicon nucleus. The tensor representations shown in this figure are based on the nuclear shielding tensor components. Note that the cation potential of the effective modifier cation increases towards the center of the

nal to the Si-NBO bonds, while becoming more shielded along the x-axis, that is parallel to the Si-NBO bonds, based on the principal nuclear shielding tensor components (Figure 13). The z-axis, which is between the two Si-NBO bonds, remained unchanged with respect to the perturbation. The trend in changing nuclear shielding anisotropy is λ_{xx} as shown in Figure 13 due to the fact that the Haeberlen convention has been ignored to keep the molecule in the axis system in which it was built. Therefore, the nuclear shielding elements are along the axis in the original axis system as indicated in Figure 3. The nuclear shielding anisotropy was found to be increasing with decreasing Si-NBO bond distance. The tensor for a cluster simulating a weak network modifying cation is shown in the top left corner of Figure 13. Based on the trends in the nuclear shielding tensor components it has been determined that the shape of the nuclear shielding tensor transforms from a football in the xz-plane that has been squeezed along y-axis to a sphere as the cation potential of the network modifying cation increases.

Therefore, the *ab initio* calculations for the $Q^{(n)}$-species clusters were determined to all be in agreement with the previous trends reported by Grimmer and coworkers [18, 19] with respect to the change in Si-NBO bond distance. Thus, the trends reported by Davis et al. [14, 15] were in agreement with the theoretical results determined by *ab initio* calculations. Therefore, as network modifying cations with greater cation potential are incorporated into the glass structure the Si-NBO bond distance should increase as indicated by the change in the nuclear shielding anisotropy.

4. Conclusions

We synthesized and analyzed natural abundance ^{29}Si 2D MAF spectra for a range of compositions of a mixed potassium/magnesium tetrasilicate glass. The spectral analysis yielded a close to equal distribution of $Q^{(3)}$ and $Q^{(4)}$ sites within the glass as expected from the stoichiometry of the glass. Two distinct nuclear shielding anisotropy patterns were determined from the simulations, centered near 84.3 ± 0.1 ppm, corresponding to pure potassium region of cation clustering, and approximately 59.9 ± 0.2 ppm, corresponding to a mixed potassium/magnesium region of cation clustering, which was proposed as a $K_{2i} \cdot Mg_i$ coordination environment. This was in agreement with the previous ^{17}O DAS results. The relative populations of each $Q^{(3)}$ site within each compositions were found to be in agreement with the binary model proposed in this paper. Therefore, a large amount of order is present within the glass relating to how the network modifying cations cluster near the non-bridging oxygens. The nuclear shielding anisotropy observed for the two unique $Q^{(3)}$ sites was consistent with established trends in which the ^{29}Si nucleus becomes more shielded with decreasing silicon non-bridging oxygen bond distance, causing an increase in nuclear shielding anisotropy when a lower field strength modifier cation is coordinated to the non-bridging oxygen.

The theoretical results obtained using *ab initio* quantum chemical calculations were found to be in good agreement with the previous experimental results [14, 15, 18, 19] that were obtained using NMR spectroscopy. Therefore, the theoretical and experimental trends both indicate that the introduction of a network modifying cation with a greater cation potential yields an increase in the magnitude nuclear shielding anisotropy due to the lengthening of the Si-NBO bond. This lengthening of the Si-NBO bonds causes a decrease in electron density near the ^{29}Si center along this bond. This decrease in electron density near the ^{29}Si center causes a decrease in shielding along the direction of decreasing electron density. Thus, network modifying cations with greater cation potential will cause an increase in the Si-NBO bond distance causing a decrease in the electron density in that direction around the ^{29}Si nucleus causing the change in the nuclear shielding tensor.

5. Acknowledgments

The authors would like to thank Professor Christopher Jaroniec for the helpful discussion on paramagnetic doping. This material is based upon

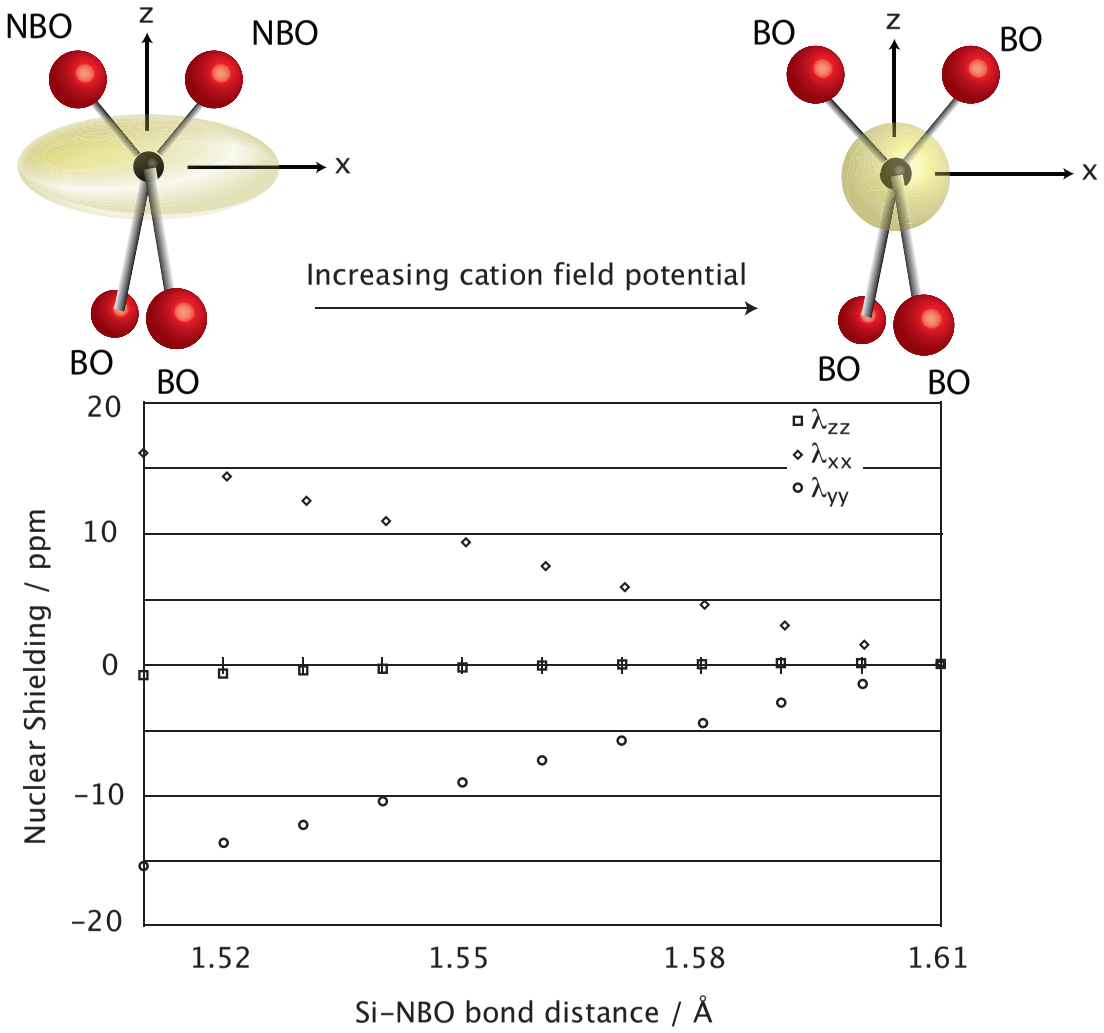

Figure 13: The *ab initio* results for the $Q^{(2)}$ cluster for Si-NBO bond distances between 1.61 Å and 1.51Å. The Haeberlen convention has been neglected for these results. Therefore, the λ values are along the respective direction from the original axis system. The nuclear shielding anisotropy for this axis system is defined as, λ_{xx} and therefore is shown to be in agreement with the previous results [14, 15, 18, 19]. The symmetric $Q^{(4)}$ cluster is shown to the top right of the graph with a spherical nuclear shielding tensor surrounding the silicon. The $Q^{(2)}$ cluster to the top left of the graph is shown for Si-NBO bond distance of 1.51 Å with the squeezed football shaped tensor surrounding the ^{29}Si nucleus. This tensor representation is based on the nuclear shielding tensor components.

work supported in part by the National Science Foundation.

[1] I. Farnan, P. J. Grandinetti, J. H. Baltisberger, J. F. Stebbins, U. Werner, M. A. Eastman, A. Pines, Quantification of the disorder in network-modified silicate glasses, Nature 358 (1992) 31–35.

[2] S. R. Elliott, The Physics of Amorphous Materials, Longman Scientific & Technical, Essex CM20 2JE, 1990.

[3] A. K. Varshneya, Fundamentals of Inorganic Glasses, Academic Press Inc., 1250 Sixth Avenue, San Diego, CA 92101, 1994.

[4] B. O. Mysen, P. Richet, Silicate Glasses and Melts, Properties and Structure, Elsevier, 2005.

[5] M. Cable, High performance glasses, in: M. Cable, J. M. Parker (Eds.), High Performance Glasses, Chapman and Hall, New York, 1992, p. 1.

[6] J. Zarzycki, Glasses and the Vitreous State, Cambridge Unversity Press, Cambridge, 1991.

[7] G. N. Greaves, A. Fontaine, P. Lagarde, D. Raoux, S. J. Gurman, Local structure of silicate glasses, Nature 293 (1981) 611–616.

[8] G. N. Greaves, X-ray absorption spectroscopy, in: Glass Science and Technology, Vol. 4B, Academic Press, 1990, pp. 1–76.

[9] M. C. Eckersley, P. H. Gaskell, A. C. Barnes, P. Chieux, Structural order in a calcium silicate glass, Nature 335 (1988) 525–527.

[10] P. H. Gaskell, M. C. Eckersley, A. C. Barnes, P. Chieux, Medium-range order in the cation distribution of a calcium silicate glass, Nature 350 (1991) 675–677.

[11] P. Florian, K. E. Vermillion, P. J. Grandinetti, I. Farnan, J. F. Stebbins, Cation distribution in mixed alkali disilicate glasses, J. Am. Chem. Soc. 118 (1996) 3493–3497.

[12] P. Zhang, C. Dunlap, P. Florian, P. J. Grandinetti, I. Farnan, J. F. Stebbins, Silicon site distributions in an alkali silicate glass derived by two-dimensional ^{29}Si nuclear magnetic resonance, J. Non. Cryst. Solids 204 (1996) 294–300.

[13] P. Zhang, P. J. Grandinetti, J. F. Stebbins, Anionic species determination in $CaSiO_3$ glass using two-dimensional ^{29}Si NMR, J. Phys. Chem. B 101 (20) (1997) 4004–4008.

[14] M. Davis, D. Kaseman, S. Parvani, K. Sanders, P. Grandinetti, P. Florian, D. Massiot, $Q^{(n)}$-species distribution in K_2O $2SiO_2$ by ^{29}Si Magic Angle Flipping NMR, J. Phys. Chem. A 114 (17) (2010) 5503–5508.

[15] M. Davis, K. J. Sanders, P. J. Grandinetti, S. J. Gaudio, S. Sen, Structural investigations of magnesium silicate glasses by ^{29}si magic-angle flipping nmr, J. Non. Cryst. Solids 357 (2011) 2787–2795.

[16] J. F. Stebbins, Effects of temperature and composition on silicate glass structure and dynamics: Si-29 NMR results, J. Non Cryst. Solids 106 (1988) 359–369.

[17] R. Dupree, D. Holland, P. W. McMillan, R. F. Pettifer, The structure of soda-silica glasses: A MAS NMR study, J. Non-Cryst. Solids 68 (1984) 399.

[18] A. R. Grimmer, E. F. Gechner, G. Molgedey, High resolution ^{29}Si NMR in solid silicates. correlations between shielding tensor and Si-O bond length, Chem. Phys. Lett. 77 (1981) 331–335.

[19] A. R. Grimmer, Correlation between individual Si-O bond lengths and the principal values of the ^{29}Si chemical-shift tensor in solid silicates, Chem. Phys. Lett. 119 (1985) 416–420.

[20] M. A. Eastman, P. J. Grandinetti, Y. K. Lee, A. Pines, Double-tuned hopping-coil probe for dynamic-angle spinning NMR, J. Magn. Reson. 98 (1992) 333–341.

[21] R. R. Ernst, G. Bodenhausen, A. Wokaun, Principles of Nuclear Magnetic Resonance in One and Two Dimensions, Oxford, Oxford, 1987.

[22] M. Mehring, High Resolution NMR Spectroscopy in Solids, Vol. 11, Springer-Verlag, Berlin, 1983.

[23] A. Bax, N. M. Szeverenyi, G. E. Maciel, Correlation of isotropic shifts and chemical shift anisotropies by two-dimensional Fourier-transform magic-angle hopping NMR spectroscopy, J. Magn. Reson. 52 (1983) 147.

[24] P. J. Grandinetti, J. H. Baltisberger, A. Llor, Y. K. Lee, U. Werner, M. A. Eastman, A. Pines, Pure absorption-mode lineshapes and sensitivity in two-dimensional dynamic angle spinning NMR, J. Magn. Reson. A 103 (1993) 72–81.

[25] H. Y. Carr, E. M. Purcell, Effects of diffusion on free precession in nuclear magnetic resonance experiments, Phys. Rev. 94 (1954) 630–638.

[26] S. Meiboom, D. Gill, Modified spin-echo method for measuring nuclear relaxation times, Rev.Sci.Instrum 29 (1958) 688.

[27] R. K. Harris, E. D. Becker, S. M. C. D. Menezes, P. Grangerd, R. E. Hoffman, K. W. Zilm, Further conventions for NMR shielding and chemical shifts, IUPAC recommendations 2008, Inorg. Chem. 3 (2008) 41–56.

[28] M. J. Frisch, G. W. Trucks, H. B. Schlegel, G. E. Scuseria, M. A. Robb, J. R. Cheeseman, J. A. Montgomery, Jr., T. Vreven, K. N. Kudin, J. C. Burant, J. M. Millam, S. S. Iyengar, J. Tomasi, V. Barone, B. Mennucci, M. Cossi, G. Scalmani, N. Rega, G. A. Petersson, H. Nakatsuji, M. Hada, M. Ehara, K. Toyota, R. Fukuda, J. Hasegawa, M. Ishida, T. Nakajima, Y. Honda, O. Kitao, H. Nakai, M. Klene, X. Li, J. E. Knox, H. P. Hratchian, J. B. Cross, V. Bakken, C. Adamo, J. Jaramillo, R. Gomperts, R. E. Stratmann, O. Yazyev, A. J. Austin, R. Cammi, C. Pomelli, J. W. Ochterski, P. Y. Ayala, K. Morokuma, G. A. Voth, P. Salvador, J. J. Dannenberg, V. G. Zakrzewski, S. Dapprich, A. D. Daniels, M. C. Strain, O. Farkas, D. K. Malick, A. D. Rabuck, K. Raghavachari, J. B. Foresman, J. V. Ortiz, Q. Cui, A. G. Baboul, S. Clifford, J. Cioslowski, B. B. Stefanov, G. Liu, A. Liashenko, P. Piskorz, I. Komaromi, R. L. Martin, D. J. Fox, T. Keith, M. A. Al-Laham, C. Y. Peng, A. Nanayakkara, M. Challacombe,

P. M. W. Gill, B. Johnson, W. Chen, M. W. Wong, C. Gonzalez, J. A. Pople, Gaussian 03, Revision C.02, Gaussian, Inc., Wallingford, CT, 2004.

[29] L. Le Page, L. D. Calvert, E. J. Gabe, Parameter variation in low-quartz between 94 and 298k, J. Phys. Chem. Solids 41 (1980) 721–725.

[30] B. Efron, Bootstrap methods: Another look at the jackknife, The Annal of Statistics 7 (1) (1979) 1–26.

[31] L. Pauling, The principles determining the structure of ionic crystals, J. Am. Chem. Soc. 51 (1929) 1010–1026.